Quasinormal scale elimination theory of the anisotropic energy spectra of atmospheric and oceanic turbulence

Boris Galperin *
College of Marine Science, University of South Florida, St. Petersburg, Florida 33701, USA

Semion Sukoriansky
Department of Mechanical Engineering, Pearlstone Center for Aeronautical Engineering Studies, Ben-Gurion University of the Negev, Beer-Sheva 84105, Israel

(Received 23 May 2019; accepted 28 April 2020; published 8 June 2020)

Progress in the rapidly expanding exploration of planetary atmospheric and oceanic environments demands an adequate qualitative and quantitative representation of various processes in anisotropic turbulence. The existing analytical spectral theories are developed for homogeneous isotropic flows. They quickly become very complicated when expanded to anisotropic flows with waves. It is possible, however, to extend one such theory, the quasinormal scale elimination (QNSE), to stably stratified and rotating flows. Here the results of the theory are compared with a large variety of oceanic and atmospheric flows. These comparisons make it possible to clarify the physics of some processes governing the atmospheric and oceanic dynamics, quantify their spectra, and investigate their latitudinal and longitudinal variabilities. Some of the main results of this analysis are that vertical and horizontal spectra of atmospheric and oceanic turbulence can be derived within QNSE analytically; there exists a quantitative affinity between atmospheric and oceanic spectra; on large scales, spectral amplitudes are determined by the extra strains that cause flow anisotropization, rather than the energy or enstrophy fluxes; and planetary circulations appear to be amenable to classification as flows with compactified (compressed) dimensionality.

DOI: 10.1103/PhysRevFluids.5.063803

I. INTRODUCTION

Planetary circulations feature huge Reynolds numbers and are turbulent on almost all scales. In addition, the action of density stratification, rotation, streamline curvature, geometric confinement, magnetic fields, etc. (i.e., the variety of external factors that can be characterized as extra strains [1]), renders these circulations anisotropic.

A systematic description of turbulence behavior in response to the impact exerted by extra strains is one of the important outstanding problems of fluid dynamics. Addressing this problem runs into difficulties from the outset because proliferation of dimensional variables hinders the application of the dimensional analysis. Direct numerical simulations are limited by the value of the resolvable Reynolds number even in relatively simple cases of channel flows [2]. Linear and nonlinear theories of anisotropic turbulence have been developed [3–6]. However, a clear understanding of the spectral behavior of such flows has proved to be elusive. Further progress relies upon the development of basic self-consistent theories that make verifiable predictions suitable for testing against a large variety of data.

*bgalperin@usf.edu

This study employs a spectral closure known as quasinormal scale elimination (QNSE), in which interactions between different physical processes, including waves, are analyzed on a scale-by-scale basis under the assumption of an infinite Reynolds number. The waves' contributions are accounted for by computing the frequency integrals over wave-generated complex poles in the course of the calculation of the renormalized Green's function [7,8].

The main purpose of QNSE is to produce expressions for the renormalized viscosities and diffusivities in anisotropic turbulence that can be used for the development of subgrid-scale (SGS) parametrization schemes suitable for practical applications either in large-eddy simulations or in models employing the Reynolds-averaged Navier-Stokes equations. In addition, QNSE provides analytical expressions for the spectra of kinetic and potential energies that are valuable on their own. They can be used to diagnose turbulence characteristics which, when measured globally by satellite networks and assimilated into numerical models, may significantly improve the models' performance.

In this paper, theoretical predictions of various spectra will be compared with measurements in atmospheric and oceanic flows. Particular attention will be given to one-dimensional (1D) spectra that quantify the turbulence anisotropy. The existing literature shows a lack of clarity with regard to spectral slopes and amplitudes of atmospheric and oceanic turbulence, their dependence on latitude, and generally their governing physics.

For vanishing extra strains or on scales on which their effect is small, a theory of anisotropic turbulence must attain its isotropic limit, e.g., the Kolmogorov theory [9–14]. This theory predicts that in the inertial range (IR), where turbulence characteristics depend on the dissipation rate ε yet are independent of the molecular kinematic viscosity ν_0, the scaling for the second-order longitudinal structure function is $D_{\rm LL}(r) = C(\varepsilon r)^{2/3}$ and the ratio of the transverse to longitudinal structure functions in incompressible (solenoidal) flows is $D_{\rm TT}(r)/D_{\rm LL}(r) = 4/3$. Here C is a constant and r is a separation distance in the physical space.

The structure functions $D_{\rm LL}(r)$ and $D_{\rm TT}(r)$ can be related to 1D, longitudinal, and transverse energy spectra $E_L(k_1)$ and $E_T(k_1)$ by the Wiener-Khinchin relationships [11]

$$D_{\rm LL}(r) = 2\int_0^\infty [1-\cos(rk_1)]E_L(k_1)dk_1, \tag{1}$$

$$D_{\rm TT}(r) = 2\int_0^\infty [1-\cos(rk_1)]E_T(k_1)dk_1, \tag{2}$$

where k_1 is a 1D vector in the longitudinal direction. By straightforward integration one can establish full expressions for the structure functions and the corresponding 1D spectra (see, e.g., [11])

$$E_L(k_1) = \tfrac{18}{55}C_K\varepsilon^{2/3}k_1^{-5/3}, \tag{3}$$

$$E_T(k_1) = \tfrac{24}{55}C_K\varepsilon^{2/3}k_1^{-5/3} \tag{4}$$

and

$$D_{\rm LL}(r) = C_L(\varepsilon r)^{2/3}, \tag{5}$$

$$D_{\rm TT}(r) = C_T(\varepsilon r)^{2/3}, \tag{6}$$

where

$$C_L = -\tfrac{18}{55}\Gamma(-2/3)C_K, \tag{7}$$

$$C_T = -\tfrac{24}{55}\Gamma(-2/3)C_K, \tag{8}$$

with $\Gamma(x)$ the Gamma function and C_K the Kolmogorov constant in the 3D Kolmogorov spectrum

$$E(k) = C_K\varepsilon^{2/3}k^{-5/3}, \tag{9}$$

where $k^2 = k_\alpha^2$ and the summation over the repeating indices is enforced. The value of C_K, as established in [15] based upon numerous experiments and observations, is

$$C_K = 1.62 \pm 0.17 \tag{10}$$

(see also the book by McComb [13]). Using (7) and (8), one computes $C_L = 2.13 \pm 0.22$ and $C_T = 2.84 \pm 0.3$. Note that the value of C_K in (10) almost perfectly agrees with the one computed in the renormalization-group (RNG) theory of turbulence when the two-parametric viscosity by Kraichnan [16] is used [17,18]. With one-parametric viscosity, one obtains $C_K \simeq 1.5$, the value that will be employed in the applications of QNSE theory in this paper.

In [14], C_L was rounded to 2. In applications, C_L varies around 2. For instance, in [19], $D_{\mathrm{LL}}(r)$ was used in data processing from Doppler radar measurements of atmospheric turbulence which gave $C_L \simeq 2.1$. This value was used several years later for computing the dissipation rate from oceanic flow velocity profiles [20–23].

The power-law dependences of the structure functions may deviate from those prescribed by Kolmogorov theory due to the effect of the intermittency (see, e.g., [12–14,24]) or the finite values of the Reynolds number (see, e.g., [25–27]). In any case, the deviations from the Kolmogorov theory are small for low-order moments such that (3) and (4) can be used as good approximations of 1D spectra from which one can estimate the dissipation rate ε.

Equations (3), (4), and (9) apply to homogeneous turbulence where the dissipation rate ε is equal to Π_ε, the rate of the energy transfer through the IR. In inhomogeneous turbulence and/or in complex flows with extra strains and waves, multiple IRs with different values of the throughput fluxes may develop. For such IRs, a more appropriate form of (9) would be the one advanced by Kraichnan [28–30],

$$E(k) = C_K \Pi_\varepsilon^{2/3} k^{-5/3}. \tag{11}$$

In a similar manner, ε should be replaced by Π_ε in the 1D spectra (3) and (4). The resulting equations are of paramount importance. In the theory of homogeneous isotropic turbulence, they establish a one-to-one correspondence between the rate of the spectral energy transfer and amplitudes of energy spectra, up to the experimentally determined coefficients. In flows with multiple IRs interlaced with regions of instabilities and enhanced and/or decreased energy fluxes, they can be used to quantify these fluxes and reconcile them with pertinent physical processes. One can expect that an accurate numerical simulation of these processes would critically depend on accommodating the values of the incoming and outgoing fluxes. Multiple Kolmogorov subranges were considered in, e.g., [31,32].

When laws of the Kolmogorov turbulence are applied to geophysical flows, it is usually implied that the assumption of homogeneity approximately holds and that ε in Kolmogorov's laws is a standard rate of viscous dissipation. In numerical models, however, laws of turbulence are applied on grid scales far exceeding the viscous scales and so Π_ε represents collective dissipation processes in large areas that encapsulate energy losses due to a variety of processes. In the oceanographic context, such processes include the topographic friction and form drag, tides, submesoscale instabilities, fronts, wave breaking, etc. They may significantly exceed the viscous dissipation measured on the microstructure [33–38]. Thus, in the oceanographic context, it is preferable to refer to Π_ε as the effective submesoscale dissipation (ESD). The precise meaning of the submesoscale will be elaborated in Sec. IX A.

Measurements reveal that in anisotropic turbulence with extra strains, laws of Kolmogorov turbulence are modified in a nontrivial way. The energy spectra acquire anisotropy while amplitudes of some 1D spectra steepen beyond Kolmogorov's slope of $-5/3$. This steepening facilitates energy accumulation in certain directions giving rise to the emergence of physical-space structures unseen in the conventional Kolmogorov turbulence. Among such structures are the horizontal layers in stably stratified oceanic flows (see, e.g., [39]), columnar vortices in rotating fluids and hurricanes in the atmosphere (see, e.g., [6,40]), and zonal jets on giant planets (see, e.g., [41]).

What determines spectral amplitudes and slopes in anisotropic flows with extra strains? Proliferation of the extra strain-related terms in the Navier-Stokes and energy equations hinders the application of the dimensional analysis, although some progress has been achieved for turbulence in stably stratified flows (see, e.g., [42]). That and other studies indicate that the characteristic for a stable stratification steep slope k_z^{-3} in the vertical direction and the associated spectral amplitude are determined by the Brunt-Väisälä frequency N rather than the energy and/or enstrophy fluxes.

In magnetohydrodynamic flows with low magnetic Reynolds number, the effect of the magnetic extra strains differs from that in stratified flows. It causes an increase of the correlation length in the magnetic field direction, turbulence quasi-two-dimensionalization, and development of the inverse energy cascade on scales larger than the forcing scale, as would be expected in forced 2D turbulence (see [43] and references therein). The application of the QNSE theory in this case reveals spectral steepening beyond the Kolmogorov slope of $-5/3$ on large scales. The spectral amplitudes are determined by the magnitude of the extra strain, which is the Joule dissipation time scale in this case, and attain a slope of $-7/3$ in all directions in a relatively weak magnetic field [43]. Slopes of -3 emerge in a strong field.

Rotating flows also exhibit spectral steepening to the slope -3 in all directions and in addition they preserve the isotropy in the plane orthogonal to the rotation vector. The isotropy between the vertical and horizontal directions is not preserved. Dating back to the pioneering study by Charney [44], the spectral steepening has been attributed to flow quasi-two-dimensionalization and the ensuing direct cascade of the potential enstrophy (PE).

An alternative explanation of the spectral steepening in rotating flows was given by the QNSE theory elaborated in [8]. It was demonstrated that the large-scale spectral amplitudes are determined by the Coriolis parameter rather than the PE fluxes. This result is in line with that in stably stratified flows and points to some general framework underlying modification of turbulence by extra strains.

One of the purposes of the present paper is to present a comparison of the QNSE results for rotating flows with the existing data. Theoretical predictions will be scrutinized against numerous observational data sets collected in the atmosphere and the ocean and good agreement between the theory and data will be demonstrated.

The steepening of the large-scale spectra in stably stratified and rotating flows and the dependence of the spectral amplitudes on the magnitude of the respective extra strains in both cases indicate that even though the physical processes are different, there is a similarity in modification of the spectral amplitudes by the extra strains. In fact, the similarity extends even further, to flows with a β effect and inverse energy cascade. In that case, a steep spectral amplitude is determined by an extra strain known as a β term and a spectrum steepens to $\beta^2 k_y^{-5}$, where k_y is the meridional component of the horizontal wave vector [41,45].

To identify the processes responsible for the spectral steepening, we note that the extra strains modify interactions of vector triads and through them alter the turbulence dynamics. Extra strains may cause the selection of preferred triad interactions, leading to energy concentration in low-dimensional subspaces [columnar vortices in rotating flows, horizontal layers in stratified flows, and zonal jets on a rotating sphere (see, e.g., [40,46,47])]. A recent review of flows with extra strains was given by Alexakis and Biferale [32].

On decreasing scales, the effect of extra strains weakens and turbulence returns to a quasi-isotropic state. Then Eqs. (3) and (4), written in terms of the energy transfer rate Π_ε rather than the dissipation rate, hold to a good approximation and can be utilized for estimating Π_ε over these scales.

Quantification of anisotropic spectra beyond dimensional analysis has important implications for rapidly developing technology of remote sensing of atmospheric and oceanic dynamics and transport properties by satellite altimetry, scatterometry, and similar tools. The QNSE theory can help to guide future data collection and interpretation of the results.

The rest of the paper is composed in the following way. Section II provides a brief description of the QNSE theory of turbulence. Section III provides a brief survey of theoretical results for stably stratified flows. Section IV elaborates QNSE results for rotating flows, while Sec. V compares

these results with atmospheric data. Sections VI and VII provide the derivation of the structure functions using the QNSE theory and compare them with observations. Section VIII extends the QNSE analysis to spherical geometry, while Sec. IX applies the QNSE results to the analysis of oceanic data. Section X embeds theoretical insight into planetary flows by combining the results for stably stratified and rotating flows. Finally, Sec. XI provides a discussion and conclusions.

II. BRIEF DESCRIPTION OF THE QNSE THEORY

The QNSE theory is formulated for a 3D turbulent flow. For stratified flows, governing equations include a vertical stabilizing temperature gradient; for rotating flows they include the Coriolis force. Flows are governed by the momentum, temperature in the case of stratification, and continuity equations in the Boussinesq approximation. A detailed derivation of the QNSE equations is given in [7,8,43,48,49] and only a brief summary is given here.

The governing equations are space-time Fourier transformed. They are strongly nonlinear as the Reynolds number Re is large on large scales. Thus, the smallest scales are those where viscous processes prevail and $\mathrm{Re} = O(1)$. The smallness of Re allows one to explore the renormalized perturbation methodology employing the dressed, or effective, or eddy viscosity and eddy diffusivity rather than their bare molecular values [50,51]. This methodology allows one to gradually coarse grain the flow domain by recursive elimination of small shells of small-scale modes and calculate the compensating effective eddy viscosity and eddy diffusivity accounting for turbulent transport on the eliminated scales. Technically, this approach follows the RNG procedure of successive scale elimination [17,52] but is distinct in some important details. Unlike the RNG method, the QNSE procedure employs no fixed point arguments. In another diversion from the RNG method, it uses a self-substitution method [48,53] to evaluate the product of slow and fast modes, i.e., the cross term, in the expansion series.

An important element of the QNSE procedure is the mapping of the velocity modes in the small shell $\Delta\Lambda$ which is subject to elimination by ensemble averaging to the Langevin equation

$$u_\alpha(\hat{k}) = G_{\alpha\beta}(\hat{k}) f_\beta(\hat{k}), \tag{12}$$

where $u_\alpha(\hat{k})$ is a space-time Fourier transform of the velocity, $\hat{k} = (\mathbf{k}, \omega)$, and $G_{\alpha\beta}(\hat{k})$ is the renormalized Green's function containing renormalized viscosity and possibly diffusivity resulting from elimination of small scales with wave numbers larger than Λ. The random force $f_\beta(\hat{k})$ is generated by nonlinear interactions as elaborated in, e.g., [30,50,54–56]. Numerous attempts to derive this force from first principles have been unsuccessful so far [50,57] and so its form has to be postulated. Physically, $f_\beta(\hat{k})$ accounts for steering of a mode k by all other modes; it is solenoidal, zero mean, white noise in time, homogeneous in time and space, and its correlation function is

$$\langle f_\alpha(\omega, \mathbf{k}) f_\beta(\omega', \mathbf{k}') \rangle = 2D(2\pi)^4 k^{-3} P_{\alpha\beta}(\mathbf{k}) \delta(\omega + \omega') \delta(\mathbf{k} + \mathbf{k}'), \tag{13}$$

where

$$P_{\alpha\beta}(\mathbf{k}) = \delta_{\alpha\beta} - \frac{k_\alpha k_\beta}{k^2} \tag{14}$$

is the projection operator that ensures the solenoidality of the velocity field. The forcing amplitude D is proportional to the energy transfer rate Π_ε. As elaborated in [7], the proportionality factor is not adjustable; it is calculated from the energy balance considerations.

As shown in [7,48], an important requirement for $\mathbf{f}$ is that $\langle f_\alpha(\mathbf{p}) f_\beta(\mathbf{q}) f_\sigma(\mathbf{k} - \mathbf{p} - \mathbf{q}) \rangle = 0$ for vector triads such that $\mathbf{p}$, $\mathbf{q}$, and $\mathbf{k} - \mathbf{p} - \mathbf{q}$ belong in the shell $\Delta\Lambda$ subject to elimination. This property alone suffices to develop a rigorous self-contained mathematical procedure of successive averaging. The force does not need to be Gaussian, although a Gaussian field would meet the above requirement. Generally, $f_\beta(\hat{k})$ could be characterized as quasinormal. The combination of the quasinormal forcing and eddy damping represented by the eddy viscosities and eddy diffusivities places QNSE in the class of quasinormal eddy-damped theories of turbulence [6,50,58,59]. Note,

however, that unlike conventional renormalized perturbation theories, the QNSE procedure does not engage the entire range of scales at once.

By straightforward computation one establishes that, under the action of stable stratification or rotation, not only does the Langevin equation (12) acquire a tensorial form but, in addition, corrections to the eddy viscosity and eddy diffusivity differ in the vertical and horizontal directions, thereby rendering renormalized viscosities and diffusivities anisotropic. In dealing with anisotropic turbulence it has been assumed that the anisotropization of the forcing $f_\beta(\hat{k})$ can be neglected such that the anisotropization of the flow field is fully reflected in the anisotropization of the Green's function. The results based upon this assumption agree well with various data sets and provide a retroactive justification to the initial assumption.

The SGS viscosity and diffusivity are well defined in flows with a wide spectral gap between the eliminated implicit or subgrid scales $k > \Lambda$ that generate the SGS parameters and explicit or resolvable scales $k < \Lambda$ upon which these parameters act [16,60,61]. In real flows, however, such a gap does not exist and so one has to introduce two-parametric viscosity and diffusivity that possess a cusplike behavior on the smallest resolvable scales $k \simeq \Lambda$ [16]. The QNSE theory employs an important simplification known as the distant interaction or spectral gap approximation in which the limit $k/\Lambda \to 0$ is taken and only the terms up to $O(k^2)$ are retained [17,56]. Essentially, this approximation enforces a spectral gap between the resolvable and subgrid scales and accordingly renormalized viscosities and diffusivities are taken as functions of Λ only. In doing so, the dependence on k, and thus the cusplike behavior of the viscosities and diffusivities, is lost. The degree of inaccuracy introduced by this approximation cannot be estimated rigorously at present. However, its utility was demonstrated by Kraichnan [54] by showing that it provides a reasonably accurate description of the effective viscosity in isotropic 3D turbulence. Additional heuristic arguments in its justification were advanced by Smith and Woodruff [56]. Upon calculation of the Green's function in (12), this equation can be used to compute the velocity correlation function and then 3D and 1D spectra.

In flows with inverse energy cascade, e.g., 2D flows, the spectral gap approximation cannot be used. Nevertheless, for such flows, the QNSE-based renormalized Green's functions can be utilized to compute the two-parametric viscosity [62].

III. QNSE RESULTS FOR STABLY STRATIFIED FLOWS

In the case of 3D flows with stable stratification, QNSE predicts both the slopes and the amplitudes of the 1D vertical spectra of the horizontal velocity, $E_1(k_3)$ and $E_2(k_3)$, and temperature $E_T(k_3)$ [or potential energy $E_p(k_3) = (\alpha g/N)^2 E_T(k_3)$, where k_3 is the vertical (or z) component of the wave vector, α is the thermal expansion coefficient, g is the gravity acceleration, and N is the Brunt-Väisälä frequency] in the limit of weak stratification [63],

$$E_1(k_3) = E_2(k_3) = \tfrac{24}{55} C_K \Pi_\varepsilon^{2/3} k_3^{-5/3} + C_B N^2 k_3^{-3}, \tag{15}$$

$$E_p(k_3) = C_T \Pi_\chi \Pi_\varepsilon^{-1/3} k_3^{-5/3} + \gamma_3 N^2 k_3^{-3}, \tag{16}$$

where $C_B = 0.214$, $C_T = 0.62$, $\gamma_3 = 0.23$, and Π_χ is the rate of the potential energy transfer analogous to Π_ε. These spectra consist of two branches, Kolmogorov and N-dependent ones, on smaller and larger scales, respectively, with the crossover scale proportional to the Ozmidov scale $L_O = (\varepsilon/N^3)^{1/2}$. Of significance, the latter branch develops in the vertical direction, along which the phase speed of the gravity wave is zero. This result is stipulated by the restriction imposed upon the wave vector triad interactions by the frequency resonance condition elaborated in, e.g., [64]. An alternative explanation of the N-dependent spectral branches was given by [65–67] based upon the hypothesis of internal gravity wave saturation. Unlike QNSE, however, this heuristic approach does not consider turbulence anisotropy and turbulence-wave interaction. In addition, it cannot predict numerical coefficients in the spectral expressions.

As shown in [63,68], Eq. (15) provides an analytical expression for the composite vertical spectrum of the horizontal velocity fluctuations observed in the ocean [69,70] and the atmosphere [71] (see also references in [68]). The QNSE-based vertical spectra of the horizontal velocity components provide a good approximation not only for those derived from atmospheric and oceanic data but also for those obtained from laboratory measurements (see [63,68] and references therein) and from computer simulations [72]. In addition, they agree well with the vertical temperature spectra obtained on Mars and Venus in [73,74] from the radio occultation data.

The spectra (15) and (16) appear as corrections to the respective Kolmogorov-Corrsin spectra in the approximation of weak stratification. As was shown in [7], the QNSE-based eddy viscosities and eddy diffusivities as well as the spectra can be derived for arbitrary stratification. The expressions in this case are very complicated and can only be dealt with numerically. However, the above expressions for the spectra seem to hold on scales far exceeding those on which they are valid according to the theory and, being analytically transparent, they are very useful for applications to stably stratified atmospheric and oceanic flows.

IV. QNSE RESULTS FOR ROTATING FLOWS

Consider 3D, neutrally stratified, incompressible (i.e., solenoidal) rotating flows in an unbounded domain. The angular velocity vector of the system rotation is aligned vertically, $\mathbf{\Omega} = \{0, 0, \Omega\}$, while $\mathbf{f} = 2\mathbf{\Omega}$ is the Coriolis vector (in spherical coordinates, its local vertical projection is $f = 2\Omega \sin\theta$, where θ is the latitude). The horizontal (or x and y) components of a wave vector $\mathbf{k}$ are k_1 and k_2. The QNSE theory yields the expressions for 1D horizontal kinetic energy (KE) spectra in the limit of a weak rotation [8],

$$E_1(k_1) = \tfrac{18}{55} C_K \Pi_\varepsilon^{2/3} k_1^{-5/3} + C_{f1} f^2 k_1^{-3}, \tag{17}$$

$$E_2(k_1) = \tfrac{24}{55} C_K \Pi_\varepsilon^{2/3} k_1^{-5/3} + C_{f2} f^2 k_1^{-3}, \tag{18}$$

where $C_{f1} = 0.0926$ and $C_{f2} = 0.24$. The vertical direction and vertical spectral component will not be considered here as they depend on stable stratification which has not been included yet in the theory along with rotation.

Rotation breaks the isotropy of 3D flows yet the spectra remain horizontally isotropic and so the two longitudinal [$E_1(k_1) \equiv E_L(k_1)$ and $E_2(k_2) \equiv E_L(k_2)$] and two transverse [$E_2(k_1) \equiv E_T(k_1)$ and $E_1(k_2) \equiv E_T(k_2)$] spectra are congruent. Note that the horizontal spectral isotropy of large-scale forced, rotating turbulence and a spectral law close to (17) were reproduced in recent direct numerical simulations in [75].

Similarly to the case of stable stratification, the spectra (17) and (18) exhibit a superposition of the Kolmogorov and flux-independent (yet f-dependent in this case) branches with the crossover scale being proportional to the Woods scale $L_\Omega = (\varepsilon/f^3)^{1/2}$, the rotational analog of the Ozmidov scale. There exists abundant evidence of the Kolmogorov range with a direct energy cascade for horizontal flows in the atmosphere (e.g., [76]) and the ocean (e.g., [77,78]), although the applicability of the Kolmogorov results to strongly anisotropic flows has been questioned. Some of these issues will be addressed later on in this paper.

The crossover scale between the Kolmogorov and rotation-dominated subranges can be computed by equating the two terms in (17). In terms of the wavelength, this scale is

$$L_c \simeq 2\pi \times 5.4^{3/4} L_\Omega \simeq 22 L_\Omega. \tag{19}$$

In solenoidal isotropic fields, $E_1(k_1)$ and $E_2(k_1)$ are related by

$$E_2(k_1) = -k_1 \frac{dE_1(k_1)}{dk_1} \tag{20}$$

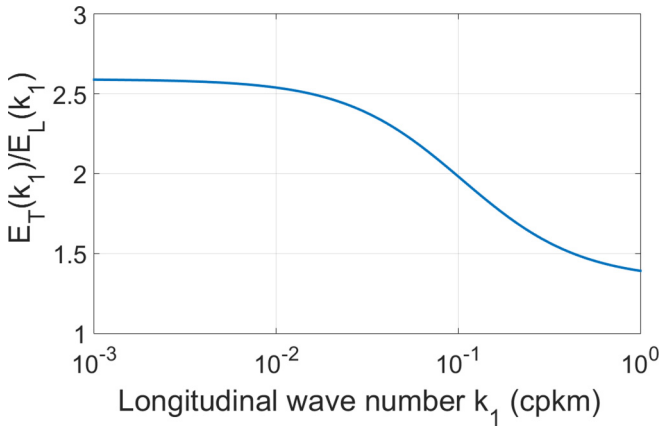

FIG. 1. Ratio $\mathcal{R} \equiv E_T(k_1)/E_L(k_1)$ based upon Eqs. (17) and (18). The latitude $\theta = 30^\circ$ N and the energy transfer rate $\Pi_\varepsilon = 5 \times 10^{-5}$ m^2 s^{-3}.

in 2D flows (see, e.g., [79]) and

$$E_2(k_1) = \frac{1}{2}\left[E_1(k_1) - k_1 \frac{dE_1(k_1)}{dk_1}\right] \tag{21}$$

in 3D flows [11]. If the 1D spectra are represented by the power laws $E_1(k_1) = A_1 k_1^{-n}$ and $E_2(k_1) = A_2 k_1^{-n}$, then for 2D and 3D solenoidal flows, $\mathcal{R}(k_1) \equiv E_2(k_1)/E_1(k_1)$ is equal to n or $(n+1)/2$, respectively. Thus, for $n = 3$, $\mathcal{R} = 3$ for 2D flows and $\mathcal{R} = 2$ for 3D flows.

In some studies, in the light of (20), the proximity of $\mathcal{R}$ to 3 has been taken as an evidence of flow two-dimensionalization on large scales [80–84]. On smaller scales, $\mathcal{R}$ decreases to about 1, which was interpreted in terms of proximity to the range dominated by internal gravity waves and describable by the Garrett-Munk spectrum [85,86]. Some observational studies (e.g., [84]) have found it difficult to explain the change of $\mathcal{R}$ with the wave number. The QNSE theory, on the other hand, offers a self-consistent framework highlighting the dependence $\mathcal{R}(k_1)$.

As discussed earlier, $\mathcal{R} = 4/3$ for the Kolmogorov subrange with $n = 5/3$. In real flows, due to a variety of factors such as the density stratification, interaction with the topography, and turbulence intermittency [87], this ratio may differ somewhat from 1.33. The dependence $\mathcal{R}(k_1)$ according to QNSE in the range of scales relevant to atmospheric turbulence as analyzed in [88] is shown in Fig. 1.

In QNSE, a flow field is solenoidal *ab initio* and so $\mathcal{R} > 1$ in both rotation-dominated and Kolmogorov ranges. Using (17) and (18), one obtains $\mathcal{R} \simeq 2.6$ on large scales, which is an intermediate value between those characteristic of isotropic 2D and 3D turbulence. A similar average value was also reported in [84] for the Southern Ocean. This outcome hints that turbulence in rotating systems and possibly some large-scale geophysical flows can be placed in the category of those with a spatial dimension larger than 2 but smaller than 3, i.e., flows with compactified dimensionality mentioned earlier in the Introduction (see also [31,89]). Such flows may feature both upscale (inverse) and downscale (direct), i.e., dual energy cascade [90–93] in the same IR. There may exist a transition, either continuous or discontinuous, between the scales with opposite cascade directions [94]. An interesting example of such a transition was discovered in the hurricane vortices where the cascade was found to have changed the sign with altitude [95].

V. COMPARISON OF QNSE RESULTS WITH ATMOSPHERIC DATA

In this section, spectra predicted by the QNSE theory are compared with those derived from atmospheric data collected by commercial aircraft during two campaigns, the Global Atmospheric

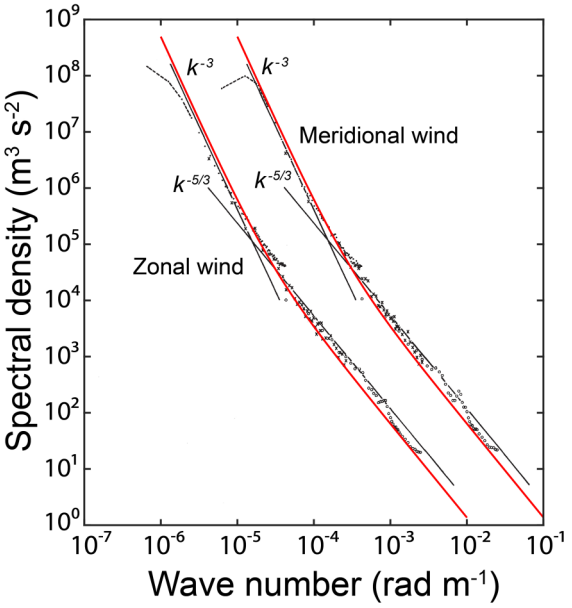

FIG. 2. Longitudinal KE spectra from [88] for flight segments in the troposphere and stratosphere in the latitudinal band 25°N–50°N. Red lines are the QNSE analytical solutions (17). The spectrum for the meridional wind is shifted one decade to the right. The latitude for the theoretical lines is $\theta = 30°$N and the energy flux is $\Pi_\varepsilon = 5 \times 10^{-5}$ m^2 s^{-3} [99]. An estimate in [100] is $\Pi_\varepsilon = 6 \times 10^{-5}$ m^2 s^{-3}. Straight black lines show Kolmogorov's $-5/3$ and synoptic -3 slopes.

Sampling Program (GASP) [96,97] and the Measurement of Ozone and Water Vapor by Airbus In-Service Aircraft (MOZAIC) [98]. For these comparisons, the axes k_1 and k_2 were aligned in the zonal (east-west) and meridional directions, respectively, and (17) and (18) were juxtaposed with the longitudinal and transverse, when available, spectra of the tropospheric and lower stratospheric aircraft winds. Generally, the spectra feature two distinct branches. On synoptic scales (between a few thousand and about 500 km), they exhibit a slope proportional to k_h^{-3}, k_h being the isotropic horizontal 1D wave number, with the amplitudes decreasing towards the equator. On mesoscales (between about 500 and 10 km), the spectra gradually transition to the classical Kolmogorov slope $k_h^{-5/3}$. The slopes and amplitudes appear to be preserved, on the average, throughout all seasons.

Figure 2 (an earlier version of this figure was reproduced as Fig. 7.21 in [6]) shows the longitudinal spectra of the zonal and meridional winds known as the Nastrom-Gage (NG) spectra vs the QNSE expression (17). The value of the energy transfer rate was estimated in [99] at $\Pi_\varepsilon = 5 \times 10^{-5}$ m^2 s^{-3}. The data-based spectral amplitudes were averaged between 25°N and 50°N, while (17) employed $\theta = 30°$N. Even though, in the visual account, the agreement between the data and the theory is quite good, the discord between the latitudinal dependence of spectral amplitudes in (17), on the one hand, and the latitudinal averaging of the data, on the other, requires some elaboration. Indeed, the accuracy of the comparison is difficult to ascertain as it is hampered by an unknown latitudinal distribution of the aircraft trajectories in the 25°N–50°N belt, uncertainty of their deviations from constant latitude circles during flights, etc.

Figure 3 provides a more detailed comparison of the latitudinal dependence of the longitudinal spectra estimated from data in [88] with (17). Both the observed and theoretical spectra exhibit a weak dependence on θ on mesoscales and strong dependence on θ on synoptic scales. Quantitatively, the agreement is satisfactory but, again, it is difficult to ascertain its details as the measurements were not designed for appraising the latitudinal dependence. The theoretical value of Π_ε was set the same as in Fig. 2.

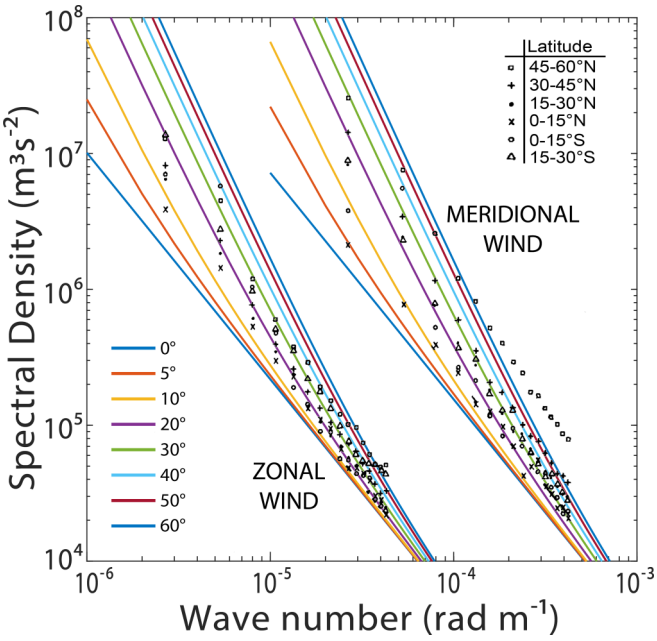

FIG. 3. Latitudinal variation of the NG spectra. The latitudes increase from bottom to top and their values are specified in the plot. The data points are from [88]. The spectra for the meridional wind are shifted one decade to the right.

The spectral branch with the -3 slope decreases towards the equator. The increasing with scale and latitude span of data spread and the range of its variability are well encapsulated in (17), both qualitatively and quantitatively. The decrease of the spectral slope towards the equator was also noted in the analyses of observational data in [97,99,101], but in the present study this phenomenon is explained and quantified. The complete disappearance of the Coriolis subrange in the equatorial regions anticipated by the theory was observed by Xu *et al.* [102] and King *et al.* [103] in their analyses of data from different scatterometers.

Various numerical simulations demonstrate the crucial role of system rotation for the formation of spectra of atmospheric turbulence with a slope steeper than Kolmogorov's $-5/3$. On the other hand, studies that excluded the Coriolis parameter featured horizontal spectra with the slope around $-5/3$ only [104,105]. When the Coriolis parameter was retained, the synoptic-range spectra not only developed the -3 slope but their amplitude was invariably close to the one predicted by (17), even in the cases with convective forcing [106,107].

In [88] and other publications by the same authors, only longitudinal NG spectra were presented. Without their transverse counterparts, however, the physical picture is incomplete. Fortunately, the MOZAIC data set contains sufficient information to evaluate both longitudinal and transverse spectra.

Figure 4 compares (17) and (18) with the longitudinal and transverse spectra as evaluated in [81] (see their Fig. 1A) using the MOZAIC data in the latitude belt between 30°N and 60°N. The details of the data selection and processing are given in the original paper. There is generally good agreement between the data-based and theoretical spectra, although the theory cannot reproduce all details of the data such as the convergence of the longitudinal and transverse spectra together on mesoscales. In the theory, the strictly enforced incompressibility ensures that the transverse spectrum is always larger than its longitudinal counterpart [11], i.e., as explained in Sec. II, $\mathcal{R}(k_1) > 1$ for all k_1.

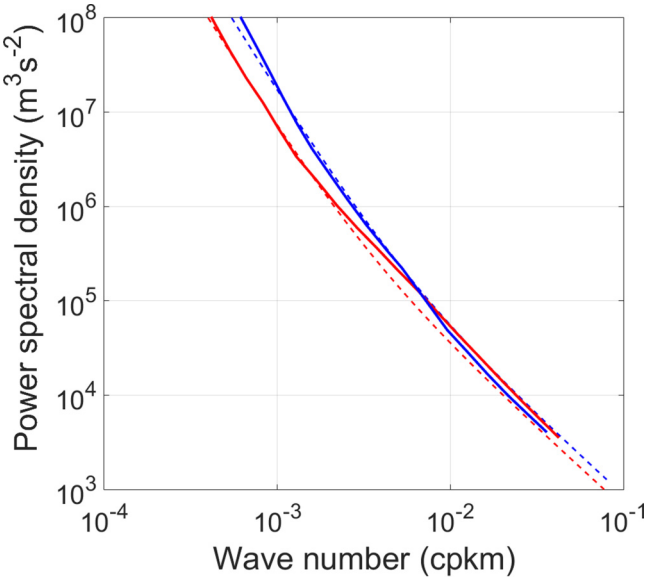

FIG. 4. Comparison of the longitudinal (red) and transverse (blue) observational spectra from [81] (solid lines) with (17) and (18) (dashed lines) for $\theta = 60°\mathrm{N}$ and $\Pi_\varepsilon = 5 \times 10^{-4}\ \mathrm{m^2\,s^{-3}}$.

Figure 5 compares (17) and (18) with the longitudinal and transverse spectra as evaluated in [108] [see their Fig. A2a]. The data set was basically the same as that used for Fig. 4, but the data selection criteria were somewhat different. To account for the air density variation with altitude, the data-based spectra were density weighed. To reflect this change, the theoretical spectra were multiplied by 0.4 $\mathrm{kg\,m^{-3}}$, which is the standard air density at 350 hPa. The differences in the data selection and processing had practically no effect on the values of the latitude θ and Π_ε reported earlier for Fig. 4. With these values, good agreement is achieved between the data-based and theoretical spectra with

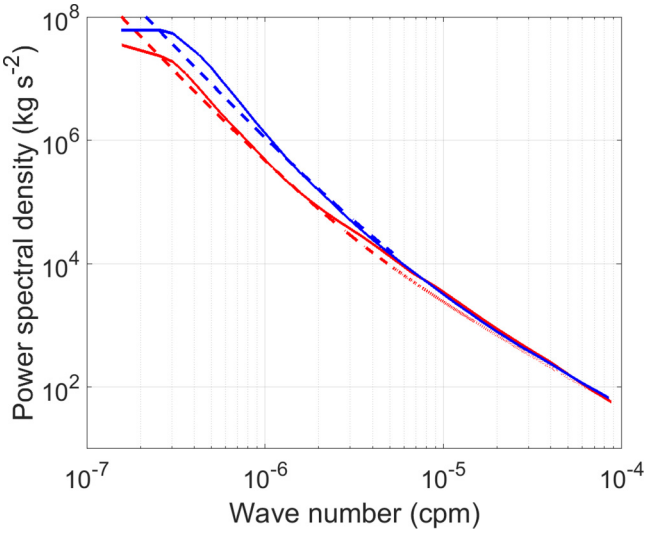

FIG. 5. Comparison of the longitudinal (red) and transverse (blue) density-weighed observational spectra from [108] (solid lines) with (17) and (18) (dashed lines) for $\theta = 60°\mathrm{N}$ and $\Pi_\varepsilon = 5.5 \times 10^{-4}\ \mathrm{m^2\,s^{-3}}$.

the limitations mentioned for Fig. 4 remaining intact. Unlike Fig. 4, however, on scales smaller than about 50 km, the longitudinal and transverse spectra in Fig. 5 become nearly indistinguishable, with the former still being a little larger than the latter. Generally, however, the agreement between the observed and theoretical Kolmogorov spectra is remarkable.

Note that, unlike Fig. 3, some analyses show that the amplitude of the stratospheric spectra increases towards the equator [109]. The exact reasons for the differences in the spectral amplitudes' behavior have not been identified yet, nor has they been confirmed in other studies such as [108]. The dissimilarities in the physical processes in the troposphere and lower stratosphere were underscored in [110], where it was shown that, while the former features the direct energy cascade, the energy flows upscale in the stratosphere. In addition, between the troposphere and stratosphere, N may sharply change by a factor of 2.

VI. SECOND-ORDER STRUCTURE FUNCTIONS

As discussed in Sec. IV, the 1D spectra $E_1(k_1) \equiv E_L(k_1)$ and $E_2(k_1) \equiv E_T(k_1)$ given by (17) and (18), respectively, are in fact the longitudinal and transverse 1D spectra in rotating flows. The second-order longitudinal and transverse structure functions $D_{\rm LL}(r)$ and $D_{\rm TT}(r)$ are related to $E_L(k_1)$ and $E_T(k_1)$ via the Wiener-Khinchin relationships (1) and (2). In a solenoidal isotropic fluid, $D_{\rm LL}(r)$ and $D_{\rm TT}(r)$ are related by a general expression

$$D_{\rm TT}(r) = D_{\rm LL}(r) + \frac{r}{d-1}\frac{dD_{\rm LL}(r)}{dr}, \tag{22}$$

valid for any spatial dimension d. For $d = 3$, this relationship was derived in [11], while for $d = 2$, it can be found in [111].

VII. STRUCTURE FUNCTIONS FOR ROTATING TURBULENCE IN THE QNSE THEORY

Using (17) and (18), Eqs. (1) and (2) can be integrated analytically to yield expressions for the second-order structure functions in the entire range of separation scales,

$$D_{\rm LL}(r) = -\tfrac{18}{55}C_K\Gamma\left(-\tfrac{2}{3}\right)(\Pi_\varepsilon r)^{2/3} + C_{f1}(fr)^2F(k_0r), \tag{23}$$

$$D_{\rm TT}(r) = -\tfrac{24}{55}C_K\Gamma\left(-\tfrac{2}{3}\right)(\Pi_\varepsilon r)^{2/3} + C_{f2}(fr)^2F(k_0r), \tag{24}$$

$$F(x) = x^{-2}[1 - \cos(x) + x\sin(x) - x^2{\rm Ci}(x)], \tag{25}$$

where ${\rm Ci}(x) = -\int_x^\infty \frac{\cos t}{t}dt$ is the cosine integral, $k_0 = 2\pi/L_0$ is the lowest wave number in the turbulence spectra, and L_0 is the maximum fluctuating scale. For small separations, (23) and (24) asymptote like $r^{2/3}$ prompting $D_{\rm TT}(r)/D_{\rm LL}(r) \to 4/3$. A comparison with data (see, for instance, Fig. 6 below) reveals that this ratio may be somewhat smaller than 1.33 on mesoscales of real atmospheric flows. These flows are spatially anisotropic due to a variety of factors such as the density stratification and interaction with the topography. In addition, finite-Reynolds-number effects and turbulence intermittency may also play a role in modifying the value of that ratio. The limit of large separations is more subtle; although the Coriolis branches of (23) and (24) become predominant with increasing r, the argument of $F(x)$, k_0r, cannot exceed a value of about 2π. Thus, the large separation asymptotic behavior for (23) and (24) is not well defined.

Figure 6 compares the QNSE-based expressions (23)–(25) with the second-order structure functions empirically fitted in [111] to the MOZAIC data. The data are treated as a unified compilation under the assumption that they represent essentially homogeneous atmospheric dynamics. As in [88], data variability with respect to altitude, latitude, season, and land or sea contrasts was disregarded. The free parameters in the analytical expressions were set to $\theta = 20^\circ$ and $\Pi_\varepsilon = 8 \times 10^{-5}\ {\rm m}^2\,{\rm s}^{-3}$.

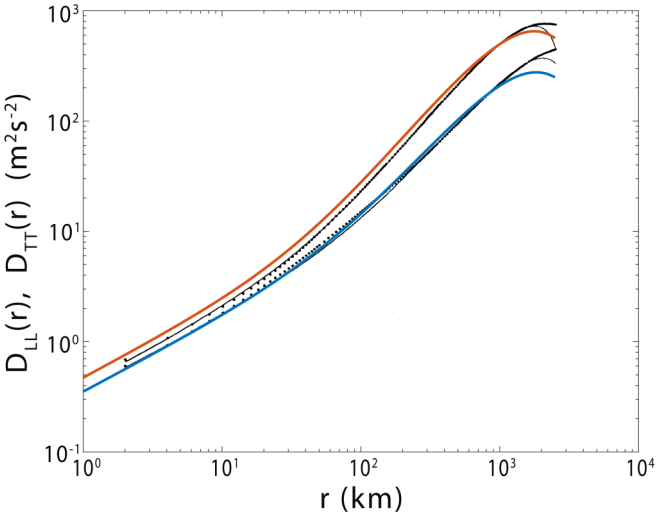

FIG. 6. Comparison of the theoretical longitudinal (blue) and transverse (red) second-order structure functions with the empirical ones (black dotted lines) computed by Lindborg [111] based upon the MOZAIC data [98]. Here $\theta = 20^\circ$ and $\Pi_\varepsilon = 8 \times 10^{-5}\ \mathrm{m}^2\,\mathrm{s}^{-3}$.

As already discussed in Sec. V, the utility of comparing latitude-averaged atmospheric data with latitude-dependent equations (23) and (24) is limited. The comparison in Fig. 6 can only be used to illustrate that the structure functions computed in [111] are approximately the same as the theoretical expressions both shapewise and magnitudewise.

As was already mentioned earlier, if the structure functions $D_{\mathrm{LL}}(r)$ and $D_{\mathrm{TT}}(r)$ can be estimated from data, then (5)–(8) can be used to evaluate Π_ε from small-scale separation profiles (see, e.g., [20–23]). The expressions for $D_{\mathrm{LL}}(r)$ and $D_{\mathrm{TT}}(r)$ are insufficient, however, for determination of the direction of the energy transfer. The sign of Π_ε can be found from the third-order structure functions. Based upon this technique, it was found that the Kolmogorov branches of the atmospheric spectra feature a downscale energy cascade [111] which is fully consistent with QNSE. However, what can be said about the energy transfer on synoptic scales?

Most of the existing theories of the synoptic range spectra utilize the paradigm of geostrophic turbulence by Charney [44] according to which a fast rotating, stably stratified 3D flow acquires dynamical properties analogous to those of purely 2D turbulence. Thus, the conservation of enstrophy (equal to the one-half of the squared vorticity) in purely two dimensions gives rise to the enstrophy range [29,112,113] with the spectrum proportional to $\Pi_\omega^{2/3}k^{-3}$ on scales smaller than the forcing scale (here Π_ω denotes the constant spectral enstrophy flux and k is the horizontal 2D wave number). Similarly, the conservation of the potential enstrophy [equal to one-half of the potential vorticity (PV) squared; PV is a vorticity modified by rotation and stratification in such a way that it becomes a materially conserved variable in geostrophic turbulence (see, e.g., [114])] gives rise to the spectrum proportional to $\Pi_\omega^{2/3}k^{-3}$ when forcing resides on large planetary scales (in this case, Π_ω denotes the spectral flux of the potential enstrophy). Lindborg and Cho [100] stated that an alternative to Charney's theory that could explain the shape of the second-order structure functions and underlying KE spectra on synoptic scales does not exist. The geostrophic turbulence underpinning is important for the dispersion processes as much as for the dynamics [115] and has been reasserted recently by Bierdel *et al.* [116], who stated that "… there is a wide consensus about the crucial role of quasi-two-dimensional balanced motions in generating the shape of the kinetic energy spectrum on synoptic scales …," and by Asselin *et al.* [117], who wrote that "[s]ynoptic-scale dynamics are typically interpreted in the light of [Charney's] theory of geostrophic turbulence, which predicts a forward enstrophy cascade along a -3 spectrum below the baroclinic injection scale."

The QNSE theory offers an alternative explanation of the spectra on synoptic scales which is readily available for a quantitative comparison with that in [111]. For the 1D variance, the equation in [111] is $E_1(k_1) = \mathcal{K}\Pi_\omega^{2/3}k_1^{-3}$, with $\mathcal{K} \simeq 0.19$ and $\Pi_\omega \simeq 1.8 \times 10^{-13}$ s^{-3}, as estimated from the MOZAIC data. Compared with (17), this yields $\Pi_\omega \propto f^3$ and $\theta \simeq 34^\circ$. Other estimates of Π_ω from atmospheric data, e.g., [109], yield similar results. The physics behind these scalings may be quite different. For comparison, the geostrophic turbulence anticipates the direct cascade of potential enstrophy. The QNSE theory, as derived for 3D turbulence, does not rely upon the assumption of a constant enstrophy flux and is capable of accommodating a dual energy cascade in a certain range of scales.

The dependence of the spectral amplitudes on the Coriolis parameter rather than the energy and/or enstrophy fluxes is a principally different result in the theory of rotating turbulence. Following Kolmogorov's theory, it has always been tacitly accepted that spectral amplitudes are ultimately determined by either of the fluxes. The computation of the fluxes is based upon the energy equation which does not contain explicit Coriolis terms. The dependence of the spectra on the Coriolis parameter may be introduced by the velocity, via the momentum equation that depends on f explicitly, and/or by the pressure-velocity correlation term whose evaluation in the physical space is very difficult. Lindborg and Cho [100] noted that the impact of the Coriolis terms on the atmospheric spectra could be profound but, due to the difficulties in evaluating the pressure-velocity correlation, they did not advance this issue any further.

The QNSE theory operates in Fourier space where the equation for the pressure is solved exactly (see [8]). This solution is used in the procedure of small-scale elimination that produces renormalized viscosities and diffusivities with an explicit dependence on f. These viscosities and diffusivities enter the Langevin equation via the Green's function rendering the velocity f dependent. In addition, the dependence of the pressure on f is reflected in the pressure-velocity correlation implicitly.

From the point of view of dimensional analysis, the spectral amplitudes in the Kolmogorov theory depend on the energy flux Π_ε because the Navier-Stokes equation does not provide an appropriate scaling parameter. On the other hand, the extra strains, when present, usually appear in the Navier-Stokes equation and so there is no reason why they should not affect the spectra explicitly. In geophysical flows, the extra strains usually support anisotropic linear waves that interact with turbulence and render it anisotropic as well. It is not surprising, therefore, that geophysical spectra reveal different scaling laws in different directions and in different ranges of scales. Proliferation of the dimensional parameters in flows with extra strains hinders the application of the dimensional analysis and so progress in this area should rely upon further advances of analytical theories of turbulence.

VIII. COMPARISON OF THE QNSE AND NG SPECTRA IN THE SPHERICAL GEOMETRY

The design and configuration of atmospheric circulation models and systems of numerical weather prediction have often been guided by their ability to reproduce the NG spectral slopes. Replication of the slopes and the crossover scale not only has become a prerequisite ensuring the correctness of the models' formulation and configuration but is often taken as a guideline for estimating the spin-up timescales, forecast error growth, and subfilterscale (or SGS) parameterizations [118]. However, since the magnitudes of the NG spectral amplitudes remained poorly constrained, the quantitative relation between the model configuration and the simulated spectra as well as the functional form and magnitude of subfilterscale parametrization has been uncertain [118–120].

By providing a quantitative explanation of the key features of the NG spectra, the QNSE theory offers a criterion suitable for assessing the accuracy of numerical models, magnitudes of spectral slopes and amplitudes, and values of the crossover scales.

In a spherical coordinate system, the meridional spectrum of the zonal velocity is in fact a transverse 1D spectrum that depends on the zonal index n. This spectrum can be represented by

Eq. (18) adapted for the spherical geometry,

$$E_Z(n) = \tfrac{24}{55} C_K \Pi_\varepsilon^{2/3} (n/R)^{-5/3} R^{-1} + C_{f2} \Omega^2 R^2 n^{-3}. \tag{26}$$

Here R is the sphere's radius and E_Z is the zonal KE per unit nondimensional index n (rather than a unit wave number) and so the dimensions of E_Z are $\mathrm{m}^2\,\mathrm{s}^{-2}$.

Figure 7 compares Eq. (26) with the results of global simulations of the troposphere and stratosphere using the nonhydrostatic atmospheric Model for Prediction Across Scales (MPAS) [118]. The agreement is quite good for the troposphere in both mesoscale and synoptic subranges but worsens in the stratosphere.

Equation (26) quantifies the dependence of E_Z on Ω. Numerical experiments in [120] demonstrated that the increase or decrease of Ω by a factor of 2 results in the increase or decrease of the amplitude of the synoptic branch of the spectrum by a factor close to 4. The mesoscale branch shows no dependence on Ω. On the other hand, as shown in [88], seasonal weather variations that drive changes in Π_ε mostly affect the mesoscale branch of the spectrum and have a small impact upon its synoptic branch. Both tendencies are in good qualitative agreement with QNSE predictions.

IX. COMPARISON OF QNSE RESULTS WITH OCEANIC DATA

As suggested by Charney [44], the laws of the geostrophic turbulence are quite general and so the expressions developed for the atmospheric spectra should be applicable to oceanic flows as well. Although the QNSE equations (17) and (18) do not imply geostrophic balance, they are quite general and include only two external parameters Π_ε and f and so, if they are germane to geophysical flows, they must provide a route to materialization of Charney's conjecture.

The applicability of the QNSE results to oceanic flows is not obvious however. On relatively large scales, oceanic flows feature an inverse energy cascade and spectral anisotropy [121–123] that result in the emergence of multiple alternating zonal jets (see, e.g., [41,124]). In addition, the magnitude of the first baroclinic Rossby radius in the ocean is much smaller than that in the atmosphere. As a consequence, the scale of the baroclinic instability and ensuing eddy forcing is also much smaller, only of the order of several hundred kilometers and less, and it decreases with increasing latitude [123].

On the other hand, the QNSE predicts that on relatively large scales, the spectral amplitudes are independent of the spectral fluxes, and if this prediction is correct, then Charney's visionary hypothesis should hold true. To test it, we utilized oceanic data obtained with the ship-mounted acoustic Doppler current profilers (ADCPs). Along-track spectra derived from the ship-mounted ADCPs and satellite altimetry have been found in agreement on scales exceeding 70 km, but on smaller scales, the satellite spectra become noisy and unrealistic (see, e.g., [84,125,126]). The comparisons in this section are aimed at clarifying qualitative and quantitative agreement between the QNSE theory and data-based spectra, the soundness of the predicted latitudinal dependence of the spectral amplitudes, and the elaboration of the KE disparity between the western and eastern basins (evident in satellite data presented in, e.g., [127–129]) in the theory despite the independence of the theoretical expressions of the longitude. Some implications of the theoretical predictions will be discussed.

A. Definition of scales

Prior to engaging in the theory-data comparisons, it is necessary to define the hierarchy of characteristic length scales. In the oceanographic literature, horizontal scales are distinguished by the proximity of the respective motions to the geostrophic balance. Thus, mostly ageostrophic scales, about 10 km and less, with the typical Rossby number $\mathrm{Ro} \equiv U/fL > 10^{-1}$, are classified as submesoscales. Nearly geostrophic scales, roughly over 10 km, for which $\mathrm{Ro} < 10^{-1}$, are classified as mesoscales. There also exist synoptic scales, with a horizontal scale of the order of the internal Rossby radius $R_d = Nh/f$, with h the thickness of the baroclinic layer. This scale, of the order

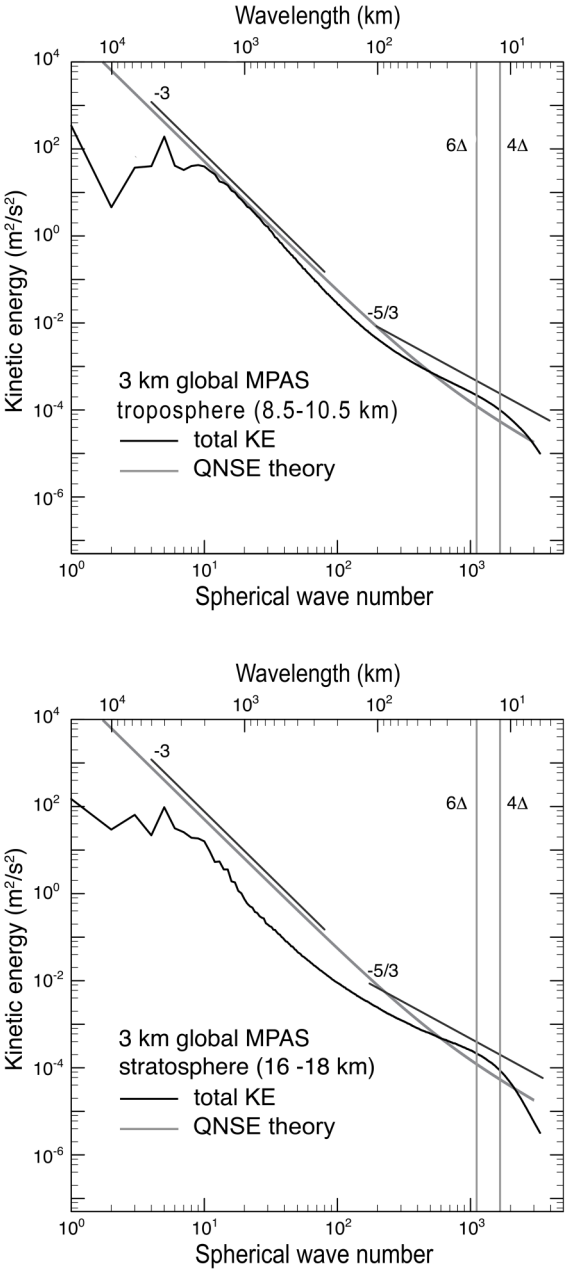

FIG. 7. The KE spectra from the 3-km MPAS global simulation for the troposphere and the stratosphere. Solid lines represent the results of simulations in [118] while the gray line is specified by Eq. (26). Vertical solid lines show the effect of the resolution as elaborated by Skamarock *et al.* [118].

of 50 km, is associated with large synoptic eddies produced by the baroclinic instability [130]. In newer terminology, these eddies are often classified as mesoscale eddies. There exist larger, highly energetic eddies known as rings that pinch from western boundary currents. Their scale may be of the order of several hundred kilometers [131].

This paper does not deal with the effects of baroclinicity; it considers ocean motions through the prism of neutrally stratified turbulence affected by rotation. For convenience, we use a different classification of oceanic scales which is based upon parameters pertinent to turbulence as expressed by the spectra (17) and (18) and the scale L_c given by (19). Galperin and Sukoriansky [132] argued that L_c plays the role of the crossover between mesoscales and submesoscales in oceanic flows. The terms submesoscales (mesoscales) will be used for scales smaller (larger) than L_c. On the mesoscales, the spectra acquire slopes steeper than Kolmogorov's $-5/3$ and approach -3. On even larger scales, the effects of the large-scale friction invoked, for instance, by the bottom drag [114] become significant and the spectra flatten out and may even decrease. These scales will be referred to as friction-dominated or simply friction scales.

Another classification of scales was considered by Qiu *et al.* [133]. They defined a scale L_t that separates unbalanced and balanced geostrophic motions. This scale was found to be useful for characterization of seasonal variability. Note that the representation of the seasonal variability in terms of L_c (see [132]) is quantitatively consistent with that in [133].

B. Latitudinal variation of oceanic spectra

1. Northwest Pacific Ocean

To study the latitudinal variation of oceanic energy spectra, we used the shipboard ADCP data presented by Qiu *et al.* [133]. The data were collected by the Japan Meteorological Society in the northwest Pacific, along the 137°E meridian, between 3°N and 34°N. Together with Kuroshio, that region contains three other subregions with different dynamical regimes. The Kuroshio, along with its southern and northern recirculating branches, occupies the band between 34°N and 28°N where it governs eddy variability. The band between 26°N and 17°N, known as the Subtropical Countercurrents (STCCs), is the southern half of the wind-driven subtropical gyre populated by multiple jets. The eddy variability in this band is due to the baroclinic instability of the STCC and westward-flowing North Equatorial Current. The latter occupies the band of latitudes between 21°N and 7°N and is quite stable due to low variability of the meridional gradient of its potential vorticity. The North Equatorial Countercurrent between 7°N and 3°N is wind driven and dynamically unstable.

Figure 8 shows that expressions (17) and (18) provide a reasonably good approximation for the slopes and amplitudes of the observational spectra at all four locations and in almost the entire interval of scales, with the exception of the largest scales where the spectra flatten out. As shown earlier, this flattening out significantly influences the geographical KE distribution. The latitudinal dependence in (17) and (18) proved to be crucial, as without the use of appropriate values of f, the agreement with the data could not be achieved. One also infers that forcing details are immaterial for the spectra's appearance on large scales, thereby confirming the theoretical result that they are largely determined by f. Changes in overall spectral slopes are stipulated by the interplay between the extents and amplitudes of the Kolmogorov and Coriolis subranges. On large scales, as f diminishes towards the equator, similarly to atmospheric flows, the steepness of spectral slopes decreases [123,134].

The rates of the energy flux Π_ε, listed in Fig. 8, yield the following values of L_c, as shown in the plates from top to bottom: 52, 126, 150, and 420 km, i.e., the submesoscale region increases with decreasing θ. Also, the values of Π_ε at all four regions are around 10^{-6} m^2 s^{-3}, which is about an order of magnitude larger than the microstructure values of ε of the order of 10^{-6}–10^{-8} m^2 s^{-3}. There exists abundant evidence that Π_ε corresponds to the direct energy cascade (see, e.g., [77,122,135]). As explained in Sec. I, Π_ε is a measure of the ESD that may far exceed the magnitude of the microstructure dissipation rate ε. The large difference between Π_ε and ε points to active submesoscale dynamics that equilibrates the imbalance.

Slopes of oceanic velocity spectra can be related to the slopes of the spectra of the sea surface height (SSH) $S^\eta(k_1)$ in the geostrophic limit. The relationship has been used to infer the details of the ocean dynamics from $S^\eta(k_1)$ [136,137]. Those spectra are often approximated by lines with a single

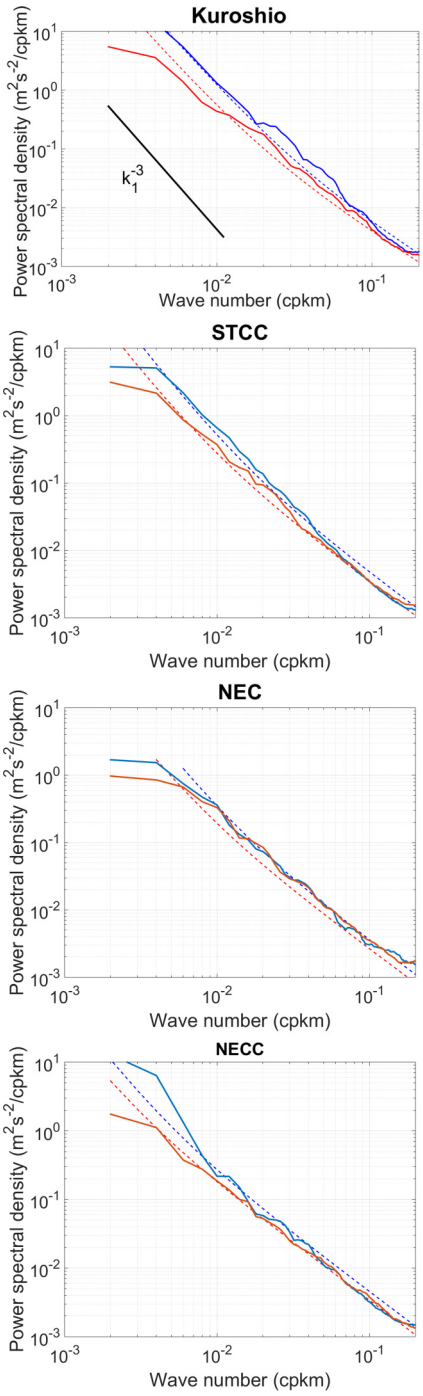

FIG. 8. Longitudinal (red) and transverse (blue) spectra obtained along 137°E in the northwest Pacific for four latitudinal regions. The latitudes are $\theta = 31°$N, 18°N, 14°N, and 8°N starting at the Kuroshio band and moving southward. The corresponding values of Π_ε are estimated at 3×10^{-6}, 3×10^{-6}, 2×10^{-6}, and 3×10^{-6} m^2 s^{-3}. The data are from [133]. The dashed red and blue lines are Eqs. (17) and (18), respectively. The top plate also shows a line with a slope k_1^{-3}.

slope, with no consideration of the two different branches. Such an approach is bound to produce spurious results for either velocity or SSH spectra because these branches are closely entwined and tend to bleed into each other, thereby affecting each other's evaluation. For illustration, the top plate in Fig. 8 shows a black line with the k_1^{-3} slope. The observed spectra approach that slope on relatively large scales but remain somewhat shallower on mesoscales and become much shallower on submesoscales. In addition, the spectral slopes alone are insufficient to infer information on ocean dynamics. Spectral amplitudes and their variation with the wave number and environmental conditions provide much more useful information for qualitative and quantitative understanding of the dynamical processes. Combined with (17) and (18), the spectral amplitudes also provide good estimates of the representative latitude and the energy flux rate Π_ε.

The latitudinal dependence of oceanic horizontal spectra was evident in the analysis of altimetric SSH and the corresponding geostrophic velocity variation considered in [129,138,139]. Simulations described in [129], particularly Fig. 11e therein, indicate that, similarly to the atmospheric spectra discussed in Sec. V, the amplitudes of the oceanic velocity spectra decrease towards the equator and approach the Kolmogorov slopes. This result points to the disappearance of the Coriolis branches as $f \to 0$.

2. Drake Passage and Antarctic Circumpolar Current

The study by Rocha *et al.* [84] analyzed the horizontal wave number spectra in the upper part of the Antarctic Circumpolar Current, 0–200 m, in the vicinity of Drake Passage, between, approximately, 55°S and 65°S. The ADCP data record is 13 years long. Along with the shipboard data, the authors also analyzed altimeter data and a high-resolution numerical simulation using the output from MITgcm.

Similarly to the NG data, the ADCP measurements detect no seasonal variability in the vicinity of Drake Passage. Seasonal variability on oceanic mesoscales and submesoscales was investigated by Galperin and Sukoriansky [132], who showed that the mesoscale variability is confined by the spectral amplitudes' dependence on the Coriolis parameter only. The submesoscale variability is governed by the variability of Π_ε.

Rocha *et al.* [84] noted that the spectra are more energetic across all scales in the range of depths between 26 and 50 m rather than at deeper layers. A close look at their Figs. 2(a)–2(c) reveals that the value of Π_ε indeed decreases with depth, pointing to the diminishing small-scale turbulence energy. At scales larger than about 100 km, the spectral amplitudes are nearly depth independent, the behavior expected of the variables that depend on f and the wave number only. The authors noted that the shapes of the spectra are nearly congruent at all depths.

Generally, compared with (17) and (18), Figs. 2(a)–2(c) in [84] exhibit somewhat lower energy. Figure 3 in that paper shows higher energy north of the mean polar front than south of it. This feature was not elaborated by the authors and it cannot be explained within the QNSE theory. It is quite possible that overall reduction of the KE density in Fig. 2 in [84] was due to the harsh navigation conditions south of the polar front that result in a lesser amount of data. North of the polar front, however, as shown in Fig. 9(a), QNSE predictions for the longitudinal and transverse spectra agree well with those inferred from the ADCP data in the entire range of scales.

In addition to a better understanding of the physics behind the atmospheric and oceanic spectra, the QNSE theory may help to improve predictions of numerical models. As an example, Fig. 9(b) compares the QNSE predictions with the results of high-resolution simulations (1/48°) using MITgcm as reported in [84]. Aside from the largest scales, the spectra on scales down to about 100 km are reproduced well, thus indicating that the primitive equations with the Coriolis terms included possess the necessary physics to replicate the large-scale turbulence. On smaller scales, however, the KE in simulations is overdamped compared with both the data and the theory (a similar overdamping was reported in, e.g., [141,142]), a fact that underscores the need for further improvement of the model and particularly representation of the mesoscale and submesoscale physics which may benefit from the QNSE results.

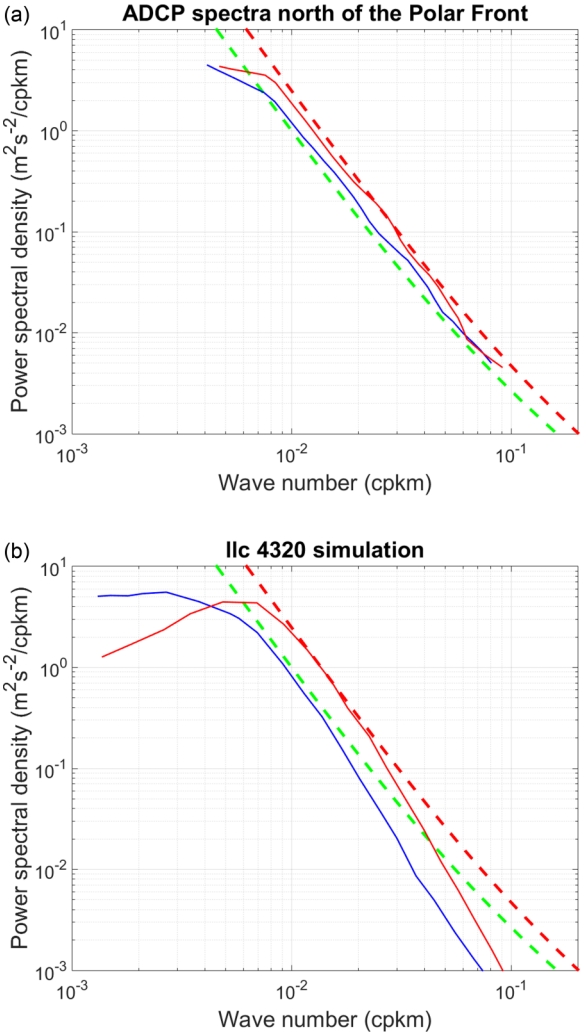

FIG. 9. (a) Longitudinal (blue solid line) and transverse (red solid line) spectra obtained from the 13 years of shipboard ADCP measurements north of the Polar Front near Drake Passage at a depth of 59–98 m. The green and red dashed lines are predictions of the QNSE theory for $\theta = 58^\circ$S and $\Pi_\varepsilon = 10^{-6}$ m^2 s^{-3}. For comparison, the microscale dissipation in the vicinity of Drake Passage is much lower, in the range of 10^{-8}–10^{-10} m^2 s^{-3} [140]. (b) Results of llc4320 simulations with MITgcm with a resolution of $1/48^\circ$. The longitudinal and transverse spectra are the blue and red solid lines, respectively. The data and simulation results are from Rocha *et al.* [84].

C. Longitudinal variation of oceanic spectra

1. Northeast Pacific Ocean

Ship-mounted ADCP data for the subtropical North Pacific Ocean in the region between 25°N and 35°N along the 140°W meridian was collected in January and February of 1997 and formed a part of the Spice data set [80,143]. This region features relatively low KE levels and will be contrasted later on with the high-energy region of the North-West Pacific, along the 137°E meridian, considered in Sec. IX B 1. A detailed description of the spectra computed for the subtropical North Pacific was given by Callies and Ferrari [80]. Figure 10 compares the observational spectra for

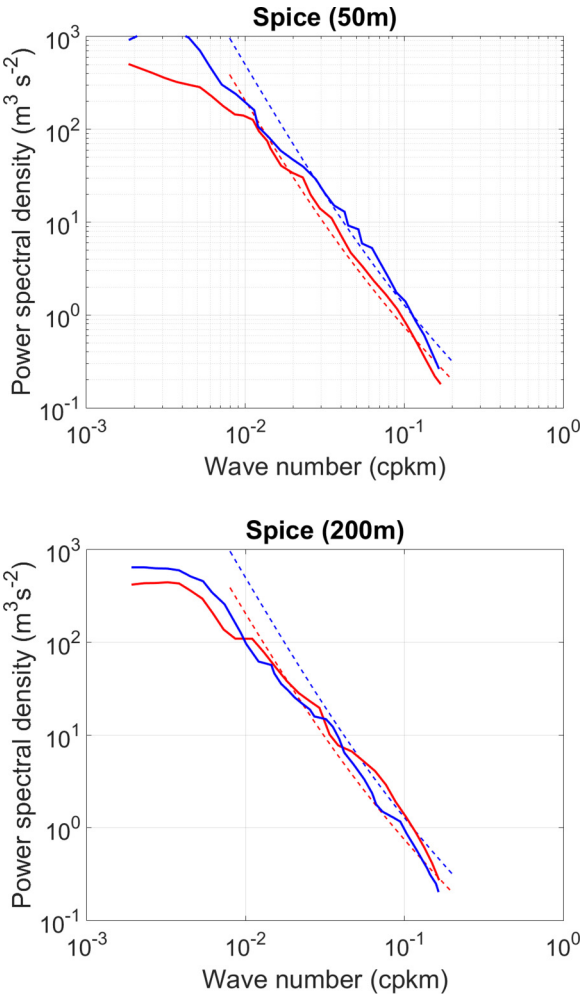

FIG. 10. Longitudinal (red) and transverse (blue) KE spectra for the subtropical North Pacific region in the mixed layer (50-m depth) and the thermocline (200-m depth) from ADCP observations [80] (thick solid lines). The dashed red and blue lines are Eqs. (17) and (18), respectively, with $\theta = 32^\circ$ and $\Pi_\varepsilon = 6.0 \times 10^{-7}$ m^2 s^{-3} for both depths.

the mixed layer (50-m depth) and the thermocline (200-m depth) with theoretical equations (17) and (18) with $\theta = 32^\circ$ and $\Pi_\varepsilon = 6 \times 10^{-7}$ m^2 s^{-3} for both depths.

Even though the observed and theoretical amplitudes are in good agreement on scales between about 5 and 50 km, in the thermocline, the longitudinal spectrum is larger than its transverse counterpart, an outcome that could be attributed to the effect of the internal waves [80]. The prevalence of the transverse spectrum on almost all scales in the mixed layer is an indication of flow incompressibility. Note that the rate of the energy transfer to the submesoscales Π_ε, which also is the ESD, remains the same at both depths yet smaller than for the energetic western Pacific, for which, as evidenced in Fig. 8, it was about five times larger.

A striking difference between the western and eastern Pacific, as obvious in Figs. 8 and 10, is the spectral behaviors on large scales. In the western basin, the observed spectra agree with the theoretical expressions (17) and (18) up to scales of about 300 km and then flatten out at a level of about 5 m^2 s^{-2}/cpkm. In the eastern basin, the observed spectra agree with the theoretical

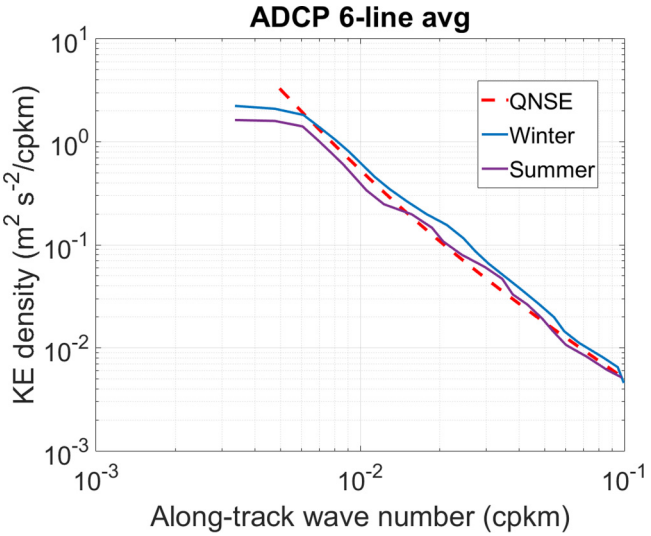

FIG. 11. Total KE spectrum at a 20-m depth for ADCP transects averaged over six lines of the CalCOFI data. The transects are season averaged for winter (December to February) and summer (June to August). Here $\theta = 30^{\circ}$N and $\Pi_\varepsilon = 5 \times 10^{-6}$ m^2 s^{-3}. The data are from Chereskin *et al.* [145].

expressions only up to scales of about 50 km, at which their slopes begin to decrease until eventually flattening out at a level of about 0.5 m^2 s^{-2}/cpkm at a scale of about 200 km. Clearly, such spectral behaviors should result in vastly different values of the KE between the western and eastern basins, which indeed has been well documented. The spectra allow one to quantify the differences. Since the observed spectra can be approximated by the theoretical expressions for scales smaller than about 50 km, these expressions can be used to estimate the energy fluxes needed for computing the SGS parameters in numerical models.

2. California Current System

The CCS region studied by Chereskin and co-workers [144,145] occupies the area farther east from the SPICE site, from 124°W to 118°W and from 30°N to 35°N. The CCS is embedded in an eastern boundary current which greatly influences its dynamics. Studies of the CCS utilized shipboard ADCP velocity observations. Similarly to the Gulf Stream (GS) region south of the GS meander considered later, the large-scale turbulence in the CCS is nearly isotropic in the horizontal, as evidenced by the nearly circular shape of the velocity variance ellipses. Comparisons of the observed and theoretical spectra are expected not only to elucidate and quantify important features of the CCS dynamics but also to contrast them to those typical of the Spice and Kuroshio sites.

Figure 11 compares QNSE predictions with KE spectra derived from the ADCP data collected from cruises by the California Cooperative Oceanic Fisheries Investigation (CalCOFI) and averaged over six lines [144]. The theoretical prediction is in reasonable agreement with the data even without seasonal adjustment of Π_ε, whose average value is estimated around 5×10^{-6} m^2 s^{-3}. For comparison, the level of the microscale dissipation in the upper 50 m of the water column is in the range of 10^{-6}–10^{-8} m^2 s^{-3} [146]. The seasonal variability is quite low and resembles the Gulf Stream's pattern, with higher turbulence levels in winters and lower ones in summers [82,132]. The magnitude of Π_ε is larger than at the Spice site and even somewhat larger than near Kuroshio, a result that points to energetic submesoscales. On large scales, up to about 200 km, the spectral amplitudes are in agreement with the QNSE predictions, reaching a level of about 2 m^2 s^{-2}/cpkm, after which the amplitudes flatten out. The ensuing values of the KE are larger than at the Spice site but smaller than in the vicinity of Kuroshio.

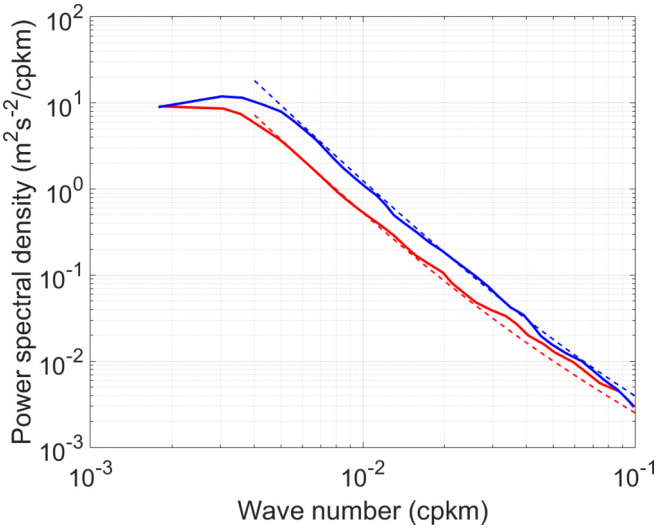

FIG. 12. Longitudinal (red) and transverse (blue) velocity spectra for a partial segment south of 36.64°N, outside of the GS meander, at a depth of 30 m from the Oleander project. The spectra are computed using the data of Wang *et al.* [125]. The thin dashed lines are Eqs. (17) and (18) with $\theta = 36^\circ$ and $\Pi_\varepsilon = 1.5 \times 10^{-6}$ m^2 s^{-3}.

3. Northwest Atlantic Ocean

In this section, the longitudinal variability of the oceanic velocity spectra is tested by comparing the data with the theoretical predictions across the North Atlantic Ocean. Two regions are considered: the vicinity of the GS and the Greenland-Portugal transects, Fourex and Ovide. Dynamically, these locations are as different as those in the western and eastern North Pacific considered in the previous sections. The former harbors the energetic western boundary current that, by virtue of barotropic and baroclinic instabilities, facilitates the emergence of large-scale eddies that provide forcing for smaller-scale turbulence. The latter location features weaker circulations on mesoscales and submesoscales.

For the GS area, a long record of the ship-mounted ADCP data has been gathered by the container motor vessel Oleander on its regular round-trip cruises between New York Harbor and Bermuda [147]. As shown by Wang *et al.* [125], velocity ellipses along the ship track exhibited a certain degree of polarization induced by the GS. The gradual weakening and eventual near disappearance of the polarization away from the GS axis pointed to the return of the eddy field and thus turbulence to the state of horizontal near isotropy.

The strong GS-induced turbulence anisotropy could not be accommodated within QNSE and so the theoretical predictions were compared with the data for the ship-track segments south of 36.64°N that excluded the GS meander. The spectra, based upon the database described by Wang *et al.* [125], were kindly recalculated for us by Wang. Figure 12 shows good agreement between these spectra and the theory at a depth of 30 m. Note that the value of $\Pi_\varepsilon = 1.5 \times 10^{-6}$ m^2 s^{-3}, emerging from this analysis, is in good agreement not only with those in the vicinity of another western boundary current, i.e., Kuroshio, but also with that in the eastern boundary current that encompasses the CCS, as shown in the previous sections.

To reduce the effect of the GS-induced anisotropy in spectral estimates, Bühler *et al.* [148] developed a mathematical procedure that was tested with the data from the Oleander project. Figure 13 compares thus evaluated longitudinal and transverse velocity spectra at a depth of 150 m with (17) and (18). While the comparison yielded a realistic latitude $\theta = 37^\circ$, the energy flux to submesoscales became enhanced tenfold compared to that at a depth of 30 m, which is quite

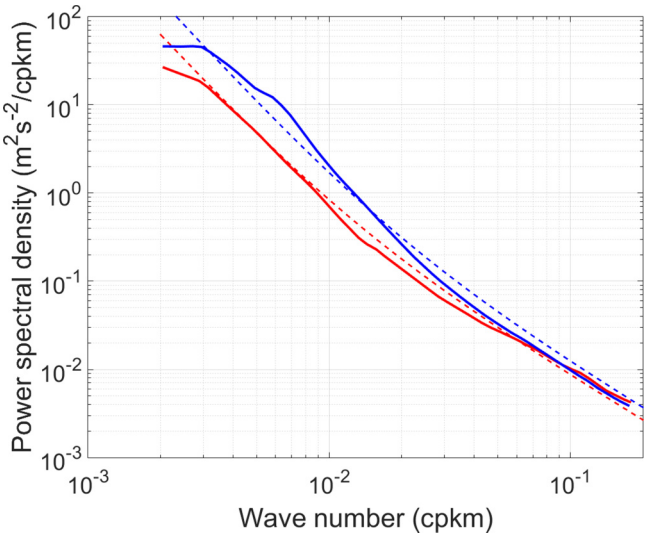

FIG. 13. Longitudinal (red) and transverse (blue) velocity spectra at a depth of 150 m from the Oleander project [148]. The thin dashed lines are Eqs. (17) and (18) with $\theta = 37^\circ$ and $\Pi_\varepsilon = 1.2 \times 10^{-5}$ m^2 s^{-3}.

unrealistic. To alleviate this outcome, the procedure reducing the effect of flow anisotropy requires further refinement.

4. Northeast Atlantic Ocean

To extend the study of the longitudinal variability of mesoscale and submesoscale oceanic turbulence, it is instructive to contrast velocity spectra in the western and eastern basins of the North Atlantic Ocean. The main currents of the North-East Atlantic Ocean drive the North Atlantic meridional overturning circulation. Compared to the North-West Atlantic, its northeast counterpart has been studied to a lesser extent. Lherminier *et al.* [126] noted that the impact of the KE level and its interaction with the large-scale circulation are not well understood. The only existing study of the upper ocean transverse velocity spectrum using the ship-mounted ADCP is that described by Gourcuff *et al.* [149] for the Greenland-Portugal transect comprised of the Ovide and Fourex sections. They cover the region between 45°W and 10°W in longitude and 60°N–40°N in latitude. The altimetry-based spectra were estimated by Gourcuff *et al.* [149] for the gridded data and by Lherminier *et al.* [126] along three Jason-1 tracks encompassing the transects and denoted traces 20, 122, and 198.

Figure 14 compares the ADCP-based transverse spectrum along the Greenland-Portugal transects presented in [149] with (18) for $\theta = 50^\circ$. The agreement is reasonably good for scales up to about 70 km, after which the slope of the observed spectrum begins to lag behind the theory. Recall that the spectra in the tropical North-East Pacific Ocean, shown in Fig. 10, exhibited a similar behavior which was attributed to a weak large-scale forcing.

The average energy flux to submesoscales throughout the Greenland-Portugal transect is about three times smaller than that for the Spice data. Even though the average value of Π_ε along the transect is smaller than at other locations considered in this section, it is still much larger than the dissipation rate ε of the order of 10^{-10} m^2 s^{-3}, estimated from the microstructure measurements by Ferron *et al.* [150] in the thermocline at a depth of about 2000 m. This value of ε is about three orders of magnitude smaller than Π_ε.

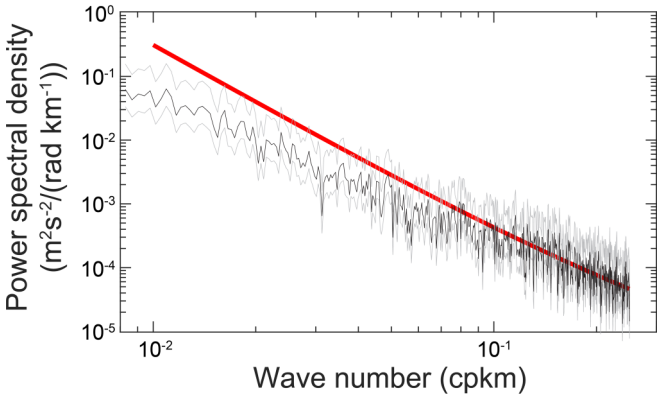

FIG. 14. Transverse velocity spectrum for the Greenland-Portugal transect. The ship-mounted ADCP spectrum (black solid line) and the 95% confidence interval estimated by the multitaper method (gray lines) are from [149]. The red line is the QNSE equation (18) with $\theta = 50^\circ$ and $\Pi_\varepsilon = 2 \times 10^{-7}$ m^2 s^{-3}.

X. COMBINED EFFECT OF f AND N

While a general QNSE theory of the combined effect of rotation and stratification has not been developed yet, some interesting conclusions can be drawn from the theory when applied to the terrestrial planets for which $f/N \ll 1$. In this case, it can be argued that stable stratification acts mostly in the vertical direction while rotation prevails in the horizontal. The QNSE shows that indeed, the Kolmogorov scaling in the horizontal is not significantly affected by stratification [63]. Consider a portion of a thin atmospheric shell whose characteristic height and horizontal length scales are H and L, respectively. The total KE of this shell can be estimated by either vertical integration of (15) to $k_3 = 2\pi/H$ or horizontal integration of (17) to $k_1 = 2\pi/L$, which should give the same energy, thus yielding $C_B N^2 H^2 \simeq C_{f1} f^2 L^2$ or $H/L \simeq f/N$. This scaling relationship was exploited in [44] and subsequent literature (e.g., [151]) via introducing the stretched coordinates $(x, y, Nz/f)$. This result is a consequence of the independence of spectra of either ε or Π_ε and the closeness of the values of C_B and C_{f1}. Hassanzadeh *et al.* [152], Aubert *et al.* [153], and Marcus *et al.* [154] studied modifications of this scaling for vortices with various environmental parameters.

XI. DISCUSSION AND CONCLUSIONS

Even though the QNSE theory in its current configuration considers either stably stratified flows with no rotation or neutrally stratified flows with constant planetary rotation, it nevertheless yields many results when applied to atmospheric and oceanic turbulence. Among those, theoretical predictions of 1D spectra in both the atmosphere and the oceans are in surprisingly good agreement with various observations. For stably stratified flows, the theoretically predicted vertical spectra of the horizontal velocity and temperature for atmospheric and oceanic turbulence on Earth and vertical temperature spectra on Venus and Mars agree well with observations.

In the case of rotating flows, the theoretical spectra replicate their observed longitudinal and transverse horizontal counterparts evaluated in the troposphere and lower stratosphere from the data assembled in the GASP and MOZAIC campaigns. In fact, QNSE provides the first derivation of the Nastrom-Gage spectra, well known in the atmospheric sciences, within an analytical theory of turbulence. Recent computational studies by Khlifi *et al.* [75] and Salhi *et al.* [155] are in agreement with the theoretical results. In addition, these results reveal the latitudinal dependence of the spectral amplitudes. Generalized for spherical coordinates, QNSE results are in good agreement with numerical simulations, replicate the Nastrom-Gage spectra in the spherical geometry, and

provide guidelines for deriving the subgrid-scale parametrizations suitable for implementation in numerical models.

In concert with the hypothesis by Charney [44], the theory demonstrates the affinity between atmospheric and oceanic spectra. In both media, turbulence is strongly affected by stable stratification and rotation. Large-scale spectral amplitudes and slopes in the directions of zero phase speed of linear waves (internal and inertial) are determined by the external parameters N or f rather than the energy or enstrophy fluxes. Due to the steepness of the spectra in these directions, these parameters dominate the total energy and allow one to recover the stretched coordinate approach introduced by Charney [44].

To draw an analogy with flows on a β plane, where turbulence with an inverse energy cascade commingles with Rossby waves, recall that the horizontal spectrum becomes anisotropic and very steep along the direction of a zero phase speed of Rossby waves. Similarly to stably stratified and rotating flows, the spectral amplitude in this direction is determined by the external parameter β ($= \Omega/R$) rather than the energy or enstrophy fluxes and the ensuing flow regime, known as zonostrophic turbulence, reveals multiple alternating zonal jets [156]. Respective structures are the horizontal layers in stably stratified and columnar vortices in rotating turbulence.

The theory makes it possible to undertake a detailed analysis of oceanic spectra on mesoscales and submesoscales. The crossover between these scales can be associated with the transition between the Coriolis parameter-dependent and Kolmogorov branches of the spectra as given by (19). The validity of the spectral results on large scales may appear questionable, however, because the weak rotation approximation implies that the range of scales L within which (17) and (18) apply is $L/L_\Omega = O(1)$. On larger scales, the renormalized viscosities cross zero values and become negative. A full solution of the QNSE equations exhibited similar behavior but a zero-viscosity limit was attained on somewhat larger scales. On the positive side, comparisons with data indicate that the analytical QNSE expressions remain valid on scales much larger than those for which the renormalized viscosities are positive. The reason for this is presently unclear. It is possible that the spectral amplitudes on scales exceeding L_Ω are set by the Coriolis parameter rather than the energy or enstrophy fluxes, as implied in the Kolmogorov theory. If so, then once set on scales close to L_Ω, the expressions for the spectral amplitudes may preserve their form on considerably larger scales. As was shown throughout the paper, various data sets indeed support the independence of the spectral amplitudes of fluxes on scales considered in the paper.

Generally, the transverse spectra almost always exceed their longitudinal counterparts, thereby pointing to the prevailing solenoidality of the flows. In some cases, however, the longitudinal spectra may be larger in certain wave number intervals. This can be associated with the signature of the wave dynamics. In either case, the spectral amplitudes are approximated by the theoretical expressions quite well. These expressions can be used to estimate Π_ε within the inertial ranges.

The theory helps to analyze the latitudinal and longitudinal variability of oceanic spectra. The former is well captured on submesoscales and mesoscales, up to the scales on which the large-scale friction processes begin to be important. The latter is facilitated by the western boundary currents and associated instabilities that, along with the large-scale friction, maintain a well-observed contrast in the KE and SSH levels between the western and eastern basins. While the spectral amplitudes on mesoscales and submesoscales are still in good agreement with the theoretical expressions, the universality is lost on large scales.

The theory singles out Π_ε as one of the most important parameters not only in homogeneous but also in inhomogeneous turbulence that encompasses submesoscales. In flows with multiple occurrences of the Kolmogorov spectra, the values of Π_ε estimated from these spectra should be used to ensure the energetic consistency between flows in different flow regimes. The Kolmogorov spectra emerging on the transition scales between the oceanic mesoscales and submesoscales can be used to assess the energy flux from the former to the latter. This energy flux is usually much larger than the rate of the viscous dissipation on the microstructure and so it serves as an effective submesoscale dissipation for the mesoscales. The assessment of the discrepancy between that flux and ε still awaits resolution.

If the observed data are intended to be used for data assimilation in numerical models, it could be quite attractive to combine a relatively accurate large-scale satellite altimetry data with the QNSE predictions on mesoscales and submesoscales. If the satellite data filtering methods can be refined such that the satellite and QNSE results can be merged on scales of about 20 km, then the QNSE-based estimates of ESD could be quite reliable and lead to a significant improvement of the SGS parametrization schemes and ultimately performance of global ocean models.

As mentioned in Sec. VII, longitudinal structure functions have been used to estimate the oceanic dissipation locally, based upon observations with tethered ADCPs [20–23]. A similar approach can be implemented to estimate the ESD using ship-mounted ADCPs for relatively small separation distances. Such a technique, along with data assimilation, may also lead to improved SGS parametrization schemes in numerical models, although the ADCP data will never be available to the same extent of geographical and temporal coverage as the satellite data.

In rotating flows, the action of a large-scale forcing facilitates the establishment of a direct energy transfer throughout scales smaller than the forcing scale. On scales of the order of the Woods scale and larger, an increasing with scale portion of the energy flux is redirected to the inverse energy cascade leading to the coexistence of simultaneous direct and inverse cascades referred to as a dual cascade. The dual cascade can potentially resolve the long-standing conundrum of identifying the path to dissipation from the large scales [157] which are otherwise dominated by the inverse cascade inherent in the classical theory of geostrophic turbulence [114].

The dynamics of turbulence is governed by triad interactions of the wave vectors which, in the case of coexistence of turbulence and waves, are modified by the resonance condition for the wave vector frequencies [12,64]. Among many others, studies in [94,158] consider a subdivision of the triad interactions into four different groups that control energy and enstrophy transfers. Imposing geometrical constraints and/or extra strains affects these groups and through them leads to modifications of transport and spectral properties of turbulence. A brief summary of such modifications and associated 3D to 2D transitions was given in [89], while an extensive review and bibliography can be found in [32].

System rotation and density stratification break the isotropy of 3D flows and confine them in the vertical direction. These effects cause the compactification of 3D geometry. Thus, geophysical flows can be categorized as those whose effective geometrical dimension is somewhere between 2 and 3. In such flows, the spectra are not necessarily related to the energy and enstrophy fluxes. An inherent complexity of these flows manifests in the fact that there are almost no studies attempting to elaborate and quantify the flux-spectra relationships. As explained in the Introduction, the dimensional analysis is not overly useful for quantification of spectral laws in flows with multiple dimensional parameters while analytical theories are scanty.

Finally, recall that in Sec. VII it was shown that the enstrophy flux as estimated from the MOZAIC spectra could be consistent with the functional dependence $\Pi_\omega \propto f^3$. More precisely, the flux, Π_ω, amounted to about 1.8×10^{-13} s^{-3} which corresponded to (17) with $\theta \simeq 34^\circ$. The proportionality between Π_ω and f^3 can be ascertained using a study by Khatri *et al.* [159] who utilized oceanic data and computer simulations to evaluate the energy and enstrophy fluxes in the upper ocean. Their horizontal 2D spectra were comparable to those in [141]. The values of Π_ω, on the other hand, estimated in 5 regions between 41°N and 52°S turned out to be some 5 orders of magnitude smaller than their atmospheric counterparts. This outcome does not support the proportionality between Π_ω and f^3 and indicates that in geophysical flows, spectral amplitudes may not be closely related to the spectral enstrophy fluxes. Thus, the physical principles underlying the connection between flow dynamics and the energy spectra may be due for some re-evaluation. The QNSE theory offers a self-consistent framework to carry it out. This framework can be enhanced by extending the theory to include a combined effect of stable stratification [7,63] and rotation.

ACKNOWLEDGMENTS

Discussions with Claude Cambon, Don Chambers, James Cho, Greg King, Eric Lindborg, and Peter Read have been most helpful. Dong-Ping Wang provided the data for the Oleander project that was used in Fig. 12 and Bo Qiu furnished the data for the northwest Pacific Ocean. Doug Myhre contributed masterful assistance with graphics. Partial funding was provided by the NASA/NOAA Ocean Surface Topography Science Team. B.G. gratefully acknowledges partial support through a University of South Florida Nexus Initiative Award. S.S. is thankful for partial support from the ISF through Grant No. 408/15.

[1] P. Bradshaw, Effects of streamline curvature on turbulent flow, NATO AGARD Report No. 169, 1973.
[2] J. C. del Álamo and J. Jiménez, Spectra of the very large anisotropic scales in turbulent channels, Phys. Fluids **15**, L41 (2003).
[3] C. Cambon and L. Jacquin, Spectral approach to non-isotropic turbulence subjected to rotation, J. Fluid Mech. **202**, 295 (1989).
[4] C. Cambon and J. F. Scott, Linear and nonlinear models of anisotropic turbulence, Annu. Rev. Fluid Mech. **31**, 1 (1999).
[5] C. Cambon, in *Theories of Turbulence*, edited by M. Oberlack and F. H. Busse (Springer Wien, New York, 2002), pp. 197–251.
[6] P. Sagaut and C. Cambon, *Homogeneous Turbulence Dynamics*, 2nd ed. (Springer, Berlin, 2018)
[7] S. Sukoriansky, B. Galperin, and I. Staroselsky, A quasinormal scale elimination model of turbulent flows with stable stratification, Phys. Fluids **17**, 085107 (2005).
[8] S. Sukoriansky and B. Galperin, QNSE theory of turbulence anisotropization and onset of the inverse energy cascade by solid body rotation, J. Fluid Mech. **805**, 384 (2016).
[9] A. N. Kolmogorov, The local structure of turbulence in incompressible viscous fluid for very large Reynolds numbers, Proc. R. Soc. London Ser. A **434**, 9 (1991).
[10] A. N. Kolmogorov, Dissipation of energy in locally isotropic turbulence, Proc. R. Soc. London Ser. A **434**, 15 (1991).
[11] A. S. Monin and A. M. Yaglom, in *Statistical Fluid Mechanics*, edited by J. L. Lumley (MIT Press, Cambridge, 1975), Vol. 2.
[12] U. Frisch, *Turbulence, The Legacy of A. N. Kolmogorov* (Cambridge University Press, Cambridge, 1995).
[13] W. D. McComb, *Homogeneous, Isotropic Turbulence* (Oxford Science, Oxford, 2014).
[14] P. A. Davidson, *Turbulence: An Introduction for Scientists and Engineers*, 2nd ed. (Oxford University Press, Oxford, 2015).
[15] K. R. Sreenivasan, On the universality of the Kolmogorov constant, Phys. Fluids **7**, 2778 (1995).
[16] R. H. Kraichnan, Eddy viscosity in two and three dimensions, J. Atmos. Sci. **33**, 1521 (1976).
[17] V. Yakhot and S. A. Orszag, Renormalization group analysis of turbulence. I. Basic theory, J. Sci. Comput. **1**, 3 (1986).
[18] W. P. Dannevik, V. Yakhot, and S. A. Orszag, Analytical theories of turbulence and the ϵ-expansion, Phys. Fluids **30**, 2021 (1987).
[19] H. Sauvageot, *Radar Meteorology* (Artech House, Boston, 1992).
[20] T. P. Rippeth, J. H. Simpson, E. Williams, and M. E. Inall, Measurement of the rates of production and dissipation of turbulent kinetic energy in an energetic tidal flow: Red Wharf Bay revisited, J. Phys. Oceanogr. **33**, 1889 (2003).
[21] P. Wiles, T. R. J. Simpson, and P. Hendricks, A novel technique for measuring the rate of turbulent dissipation in the marine environment, Geophys. Res. Lett. **33**, L21608 (2006).
[22] N. S. Lucas, J. H. Simpson, T. P. Rippeth, and C. P. Old, Measuring turbulent dissipation using a tethered ADCP, J. Atmos. Ocean. Technol. **31**, 1826 (2014).

[23] B. D. Scannell, T. P. Rippeth, J. H. Simpson, J. A. Polton, and J. E. Hopkins, Correcting surface wave bias in structure function estimates of turbulent kinetic energy dissipation rate, J. Atmos. Ocean. Technol. **34**, 2257 (2017).
[24] G. Boffetta, A. Mazzino, and A. Vulpiani, Twenty-five years of multifractals in fully developed turbulence: A tribute to Giovanni Paladin, J. Phys. A: Math. Theor. **41**, 363001 (2008).
[25] W. D. McComb, S. R. Yoffe, M. F. Linkmann, and A. Berera, Spectral analysis of structure functions and their scaling exponents in forced isotropic turbulence, Phys. Rev. E **90**, 053010 (2014).
[26] R. A. Antonia, S. L. Tang, L. Djenidi, and Y. Zhou, Finite Reynolds number effect and the 4/5 law, Phys. Rev. Fluids **4**, 084602 (2019).
[27] S. Tang, R. A. Antonia, L. Djenidi, and Y. Zhou, Can small-scale turbulence approach a quasi-universal state? Phys. Rev. Fluids **4**, 024607 (2019).
[28] R. H. Kraichnan, Decay of isotropic turbulence in the direct-interaction approximation, Phys. Fluids **7**, 1030 (1964).
[29] R. H. Kraichnan, Inertial ranges in two-dimensional turbulence, Phys. Fluids **10**, 1417 (1967).
[30] R. H. Kraichnan, Inertial-range transfer in two- and three-dimensional turbulence, J. Fluid Mech. **47**, 525 (1971).
[31] A. Celani, S. Musacchio, and D. Vincenzi, Turbulence in More than Two and Less than Three Dimensions, Phys. Rev. Lett. **104**, 184506 (2010).
[32] A. Alexakis and L. Biferale, Cascades and transitions in turbulent flows, Phys. Rep. **767–769**, 1 (2018).
[33] D. P. Winkel, M. C. Gregg, and T. B. Sanford, Patterns of shear and turbulence across the Florida Current, J. Phys. Oceanogr. **32**, 3269 (2002).
[34] R. Inoue, M. C. Gregg, and R. R. Harcourt, Mixing rates across the Gulf Stream, Part I: On the formation of Eighteen Degree Water, J. Mar. Res. **68**, 643 (2010).
[35] E. D'Asaro, C. Lee, L. Rainville, R. Harcourt, and L. Thomas, Enhanced turbulence and energy dissipation at ocean fronts, Science **332**, 318 (2011).
[36] A. Shcherbina, M. Sundermeyer, E. Kunze, E. D'Asaro, G. Badin, D. Birch, A.-M. E. Brunner-Suzuki, J. Callies, B. K. Cervantes, M. Claret *et al.*, The Latmix summer campaign, Bull. Am. Meteorol. Soc. **96**, 1257 (2015).
[37] J. Gula, M. J. Molemaker, and J. C. McWilliams, Topographic generation of submesoscale centrifugal instability and energy dissipation, Nat. Commun. **7**, 12811 (2016).
[38] T. Nagai, D. Hasegawa, T. Tanaka, H. Nakamura, E. Tsutsumi, R. Inoue, and T. Yamashiro, First evidence of coherent bands of strong turbulent layers associated with high-wavenumber internal-wave shear in the upstream Kuroshio, Sci. Rep. **7**, 14555 (2017).
[39] O. M. Phillips, *The Dynamics of the Upper Ocean*, 2nd ed. (Cambridge University Press, Cambridge, 1977).
[40] L. M. Smith and F. Waleffe, Generation of slow large scales in forced rotating stratified turbulence, J. Fluid Mech. **451**, 145 (2002).
[41] *Zonal Jets: Phenomenology, Genesis, and Physics*, edited by B. Galperin and P. L. Read (Cambridge University Press, Cambridge, 2019).
[42] P. Billant and J.-M. Chomaz, Self-similarity of strongly stratified inviscid flows, Phys. Fluids **13**, 1645 (2001).
[43] S. Sukoriansky and E. Zemach, Theoretical study of anisotropic MHD turbulence with low magnetic Reynolds number, Phys. Scr. **91**, 034001 (2016).
[44] J. G. Charney, Geostrophic turbulence, J. Atmos. Sci. **28**, 1087 (1971).
[45] A. Chekhlov, S. A. Orszag, S. Sukoriansky, B. Galperin, and I. Staroselsky, The effect of small-scale forcing on large-scale structures in two-dimensional flows, Physica D **98**, 321 (1996).
[46] G. Holloway and M. C. Hendershott, Stochastic closure for nonlinear Rossby waves, J. Fluid Mech. **82**, 747 (1977).
[47] H.-P. Huang, B. Galperin, and S. Sukoriansky, Anisotropic spectra in two-dimensional turbulence on the surface of a rotating sphere, Phys. Fluids **13**, 225 (2001).
[48] S. Sukoriansky, B. Galperin, and I. Staroselsky, Cross-terms and ϵ-expansion in RNG theory of turbulence, Fluid Dyn. Res. **33**, 319 (2003).

[49] S. Sukoriansky, B. Galperin, and V. Perov, A quasi-normal scale elimination model of turbulence and its application to stably stratified flows, Nonlinear Process. Geophys. **13**, 9 (2006).
[50] W. D. McComb, *The Physics of Fluid Turbulence* (Oxford University Press, Oxford, 1991).
[51] W. D. McComb, Theory of turbulence, Rep. Prog. Phys. **58**, 1117 (1995).
[52] D. Forster, D. R. Nelson, and M. J. Stephen, Large distance and long-time properties of a randomly stirred fluid, Phys. Rev. A **16**, 732 (1977).
[53] A. Berera and S. R. Yoffe, Reexamination of the infrared properties of randomly stirred hydrodynamics, Phys. Rev. E **82**, 066304 (2010).
[54] R. H. Kraichnan, An interpretation of the Yakhot-Orszag turbulence theory, Phys. Fluids **30**, 2400 (1987).
[55] M. Lesieur, *Turbulence in Fluids*, 3rd ed. (Kluwer, Dordrecht, 1997).
[56] L. M. Smith and S. L. Woodruff, Renormalization-group analysis of turbulence, Annu. Rev. Fluid Mech. **30**, 275 (1998).
[57] V. M. Canuto and M. S. Dubovikov, Dynamical model for turbulence: I. General formalism, Phys. Fluids **8**, 571 (1996).
[58] S. A. Orszag, in *Les Houches Summer School in Physics*, edited by R. Balian and J.-L. Peabe (Gordon and Breach, New York, 1977), pp. 237–374.
[59] J. R. Chasnov, Simulation of the Kolmogorov inertial subrange using an improved subgrid model, Phys. Fluids A **3**, 188 (1991).
[60] G. K. Batchelor, *An Introduction to Fluid Dynamics* (Cambridge University Press, Cambridge, 1970).
[61] H. Tennekes and J. L. Lumley, *A First Course in Turbulence* (MIT Press, Cambridge, 1972).
[62] A. Chekhlov, S. A. Orszag, S. Sukoriansky, B. Galperin, and I. Staroselsky, Direct numerical simulation tests of eddy viscosity in two dimensions, Phys. Fluids **6**, 2548 (1994).
[63] S. Sukoriansky and B. Galperin, An analytical theory of the buoyancy—Kolmogorov subrange transition in turbulent flows with stable stratification, Philos. Trans. R. Soc. A **371**, 20120212 (2013).
[64] G. Holloway, Eddies, waves, circulation, and mixing—Statistical geofluid mechanics, Annu. Rev. Fluid Mech. **18**, 91 (1986).
[65] E. M. Dewan, Stratospheric wave spectra resembling turbulence, Science **204**, 832 (1979).
[66] E. M. Dewan and R. E. Good, Saturation and the "universal" spectrum for vertical profiles of horizontal scalar winds in the atmosphere, J. Geophys. Res. **91**, 2742 (1986).
[67] T. Tsuda, T. E. VanZandt, M. Mizumoto, S. Kato, and S. Fukao, Spectral analysis of temperature and Brunt-Väisälä frequency fluctuations observed by radiosondes, J. Geophys. Res. **96**, 17265 (1991).
[68] B. Galperin and S. Sukoriansky, Geophysical flows with anisotropic turbulence and dispersive waves: Flows with stable stratification, Ocean Dyn. **60**, 1319 (2010).
[69] A. E. Gargett, P. J. Hendricks, T. B. Sanford, T. R. Osborn, and A. J. Williams, A composite spectrum of vertical shear in the upper ocean, J. Phys. Oceanogr. **11**, 1258 (1981).
[70] M. C. Gregg, D. P. Winkel, and T. B. Sanford, Varieties of fully resolved spectra of vertical shear, J. Phys. Oceanogr. **23**, 124 (1993).
[71] S. A. Smith, D. C. Fritts, and T. E. VanZandt, Evidence for saturated spectrum of atmospheric gravity waves, J. Atmos. Sci. **44**, 1404 (1987).
[72] A. Maffioli, Vertical spectra of stratified turbulence at large horizontal scales, Phys. Rev. Fluids **2**, 104802 (2017).
[73] H. Ando, T. Imamura, and T. Tsuda, Vertical wavenumber spectra of gravity waves in the Martian atmosphere obtained from *Mars Global Surveyor* radio occultation data, J. Atmos. Sci. **69**, 2906 (2012).
[74] H. Ando, T. Imamura, T. Tsuda, S. Tellmann, M. Pätzold, and B. Häusler, Vertical wavenumber spectra of gravity waves in the Venus atmosphere obtained from *Venus Express* radio occultation data: Evidence for saturation, J. Atmos. Sci. **72**, 2318 (2015).
[75] A. Khlifi, A. Salhi, S. Nasraoui, F. Godeferd, and C. Cambon, Spectral energy scaling in precessing turbulence, Phys. Rev. E **98**, 011102(R) (2018).
[76] M. Q. Menchaca and D. R. Durran, The influence of gravity waves on the slope of the kinetic energy spectrum in simulations of idealized midlatitude cyclones, J. Atmos. Sci. **76**, 2103 (2019).

[77] A. C. Poje, T. M. Özgökmen, D. J. Bogucki, and A. D. Kirwan, Jr., Evidence of a forward energy cascade and Kolmogorov self-similarity in submesoscale ocean surface drifter observations, Phys. Fluids **29**, 020701 (2017).
[78] D. Balwada, J. H. LaCasce, and K. G. Speer, Scale-dependent distribution of kinetic energy from surface drifters in the Gulf of Mexico, Geophys. Res. Lett. **43**, 10856 (2016).
[79] C. E. Leith, Atmospheric predictability and two dimensional turbulence, J. Atmos. Sci. **28**, 145 (1971).
[80] J. Callies and R. Ferrari, Interpreting energy and tracer spectra of upper-ocean turbulence in the submesoscale range (1–200 km), J. Phys. Oceanogr. **43**, 2456 (2013).
[81] J. Callies, R. Ferrari, and O. Bühler, Transition from geostrophic turbulence to inertia-gravity waves in the atmospheric energy spectrum, Proc. Natl. Acad. Sci. USA **111**, 17033 (2014).
[82] J. Callies, R. Ferrari, J. M. Klymak, and J. Gula, Seasonality in submesoscale turbulence, Nat. Commun. **6**, 6862 (2015).
[83] O. Bühler, J. Callies, and R. Ferrari, Wave-vortex decomposition of one-dimensional ship-track data, J. Fluid Mech. **756**, 1007 (2014).
[84] C. B. Rocha, T. K. Chereskin, S. T. Gille, and D. Menemenlis, Mesoscale to submesoscale wavenumber spectra in Drake Passage, J. Phys. Oceanogr. **46**, 601 (2016).
[85] C. Garrett and W. Munk, Internal waves in the ocean, Annu. Rev. Fluid Mech. **11**, 339 (1979).
[86] W. Munk, in *Evolution of Physical Oceanography: Scientific Surveys in Honor of Henry Stommel*, edited by B. A. Warren and C. Wunsch (MIT Press, Cambridge, 1981), pp. 264–291.
[87] A. E. Gledzer, E. B. Gledzer, A. A. Khapaev, and O. G. Chkhetiani, Effect of three-dimensional structures on the dynamics of turbulence in thin layers of fluid in a laboratory experiment, Izv. Atmos. Ocean. Phys. **49**, 187 (2013).
[88] G. D. Nastrom and K. S. Gage, A climatology of atmospheric wave number spectra of wind and temperature observed by commercial aircraft, J. Atmos. Sci. **42**, 950 (1985).
[89] R. E. Ecke, From 2D to 3D in fluid turbulence: Unexpected critical transitions, J. Fluid Mech. **828**, 1 (2017).
[90] E. Deusebio, G. Boffetta, E. Lindborg, and S. Musacchio, Dimensional transition in rotating turbulence, Phys. Rev. E **90**, 023005 (2014).
[91] B. Qiu, S. Chen, P. Klein, H. Sasaki, and Y. Sasai, Seasonal mesoscale and submesoscale eddy variability along the North Pacific subtropical countercurrent, J. Phys. Oceanogr. **44**, 3079 (2014).
[92] A. Pouquet, R. Marino, P. D. Mininni, and D. Rosenberg, Dual constant-flux energy cascades to both large scales and small scales, Phys. Fluids **29**, 111108 (2017).
[93] G. P. King, J. Vogelzang, and A. Stoffelen, Upscale and downscale energy transfer over the tropical Pacific revealed by scatterometer winds, J. Geophys. Res. Oceans **120**, 346 (2015).
[94] G. Sahoo, A. Alexakis, and L. Biferale, Discontinous Transitions from Direct to Inverse Cascade in Three-Dimensional Turbulence, Phys. Rev. Lett. **118**, 164501 (2017).
[95] D. Byrne and J. A. Zhang, Height-dependent transition from 3-D to 2-D turbulence in the hurricane boundary layer, Geophys. Res. Lett. **40**, 1439 (2013).
[96] P. Perkins and U. R. C. Gustaffson, An automated atmospheric sampling system operating on 747 airliners, NASA Report No. NASA TM X-71790, 1975.
[97] G. D. Nastrom, K. S. Gage, and W. H. Jasperson, Kinetic energy spectrum of large- and mesoscale atmospheric processes, Nature (London) **310**, 36 (1984).
[98] A. Marenco, V. Thouret, P. Nédélec, H. Smith, M. Helten, D. Kley, F. Karcher, P. Simon, K. Law, J. Pyle, G. Poschmann, R. Von Wrede, C. Hume, and T. Cook, Measurements of ozone and water vapor by Airbus in-service aircraft: The MOZAIC airborne program, an overview, J. Geophys. Res. Atmos. **103**, 25631 (1998).
[99] R. Frehlich and R. Sharman, Climatology of velocity and temperature turbulence statistics determined from rawinsonde and ACARS/AMDAR data, J. Appl. Meteor. Climat. **49**, 1149 (2010).
[100] E. Lindborg and J. Y. N. Cho, Horizontal velocity structure functions in the upper troposphere and lower stratosphere: 2. Theoretical considerations, J. Geophys. Res. **106**, 10233 (2001).

[101] J. Patoux and R. A. Brown, Spectral analysis of QuikSCAT surface winds and two-dimensional turbulence, J. Geophys. Res. **106**, 23,995 (2001).
[102] Y. Xu, L.-L. Fu, and R. Tulloch, The global characteristics of the wavenumber spectrum of ocean surface wind, J. Phys. Oceanogr. **41**, 1576 (2011).
[103] G. P. King, J. Vogelzang, and A. Stoffelen, Second-order structure function analysis of scatterometer winds over the Tropical Pacific, J. Geophys. Res. Oceans **120**, 362 (2015).
[104] D. R. Durran and J. A. Weyn, Thunderstorms do not get butterflies, Bull. Am. Meteor. Soc. **97**, 237 (2016).
[105] J. A. Weyn and D. R. Durran, The dependence of the predictability of mesoscale convective systems on the horizontal scale and amplitude of initial errors in idealized simulations, J. Atmos. Sci. **74**, 2191 (2017).
[106] M. L. Waite and C. Snyder, Mesoscale energy spectra of moist baroclinic waves, J. Atmos. Sci. **70**, 1242 (2013).
[107] Y. Q. Sun and F. Zhang, Intrinsic versus practical limits of atmospheric predictability and the significance of the butterfly effect, J. Atmos. Sci. **73**, 1419 (2016).
[108] J. Callies, O. Bühler, and R. Ferrari, The dynamics of mesoscale winds in the upper troposphere and lower stratosphere, J. Atmos. Sci. **73**, 4853 (2016).
[109] J. Y. N. Cho and E. Lindborg, Horizontal velocity structure functions in the upper troposphere and lower stratosphere 1. Observations, J. Geophys. Res. **106**, 10223 (2001).
[110] D. Faranda, V. Lembo, M. Iyer, D. Kuzzay, S. Chibbaro, F. Daviaud, and B. Dubrulle, Computation and characterization of local subfilter-scale energy transfers in atmospheric flows, J. Atmos. Sci. **75**, 2175 (2018).
[111] E. Lindborg, Can the atmospheric kinetic energy spectrum be explained by two-dimensional turbulence? J. Fluid Mech. **388**, 259 (1999).
[112] G. K. Batchelor, Computation of the energy spectrum in homogeneous two-dimensional turbulence, Phys. Fluids **12**, 233 (1969).
[113] C. E. Leith, Diffusion approximation for two-dimensional turbulence, Phys. Fluids **11**, 671 (1968).
[114] G. K. Vallis, *Atmospheric and Oceanic Fluid Dynamics* (Cambridge University Press, Cambridge, U.K., 2006).
[115] F. J. Beron-Vera and J. H. LaCasce, Statistics of simulated and observed pair separations in the Gulf of Mexico, J. Phys. Oceanogr. **46**, 2183 (2016).
[116] L. Bierdel, C. Snyder, S.-H. Park, and W. C. Skamarock, Accuracy of rotational and divergent kinetic energy spectra diagnosed from flight-track winds, J. Atmos. Sci. **73**, 3273 (2016).
[117] O. Asselin, P. Bartello, and D. N. Straub, On Boussinesq dynamics near the tropopause, J. Atmos. Sci. **75**, 571 (2018).
[118] W. C. Skamarock, S.-H. Park, J. B. Klemp, and C. Snyder, Atmospheric kinetic energy spectra from global high-resolution nonhydrostatic simulations, J. Atmos. Sci. **71**, 4369 (2014).
[119] Y. O. Takahashi, K. Hamilton, and W. Ohfuchi, Explicit global simulation of the mesoscale spectrum of atmospheric motions, Geophys. Res. Lett. **33**, L12812 (2006).
[120] K. Hamilton, Y. O. Takahashi, and W. Ohfuchi, Mesoscale spectrum of atmospheric motions investigated in a very fine resolution global general circulation model, J. Geophys. Res. **113**, D18110 (2008).
[121] H.-P. Huang, A. Kaplan, E. N. Curchitser, and N. A. Maximenko, The degree of anisotropy for mid-ocean currents from satellite observations and an eddy-permitting model simulation, J. Geophys. Res. **112**, C09005 (2007).
[122] S. Wang, Z. Liu, and C. Pang, Geographical distribution and anisotropy of the inverse kinetic energy cascade, and its role in the eddy equilibrium processes, J. Geophys. Res. Oceans **120**, 4891 (2015).
[123] S. Wang, F. Qiao, D. Dai, and X. Zhou, Anisotropy of the sea surface height wavenumber spectrum from altimeter observations, Sci. Rep. **9**, 15896 (2019).
[124] B. Galperin, H. Nakano, H.-P. Huang, and S. Sukoriansky, The ubiquitous zonal jets in the atmospheres of giant planets and Earth's oceans, Geophys. Res. Lett. **31**, L13303 (2004).

[125] D.-P. Wang, C. N. Flagg, K. Donohue, and H. T. Rossby, Wavenumber spectrum in the Gulf Stream from shipboard ADCP observations and comparison with altimetry measurements, J. Phys. Oceanogr. **40**, 840 (2010).
[126] P. Lherminier, P. Klein, and L. Dumas, Mesoscale turbulence properties in the North-East Atlantic from altimetry and ADCP observations (European Geosciences Union, Vienna, 2012).
[127] C. Wunsch and D. Stammer, Satellite altimetry, the marine geoid, and the ocean general circulation, Annu. Rev. Earth Planet. Sci. **26**, 219 (1998).
[128] H. Sasaki and P. Klein, SSH wavenumber spectra in the North Pacific from a high-resolution realistic simulation, J. Phys. Oceanogr. **42**, 1233 (2012).
[129] S. Biri, N. Serra, M. G. Scharffenberg, and D. Stammer, Atlantic sea surface height and velocity spectra inferred from satellite altimetry and a hierarchy of numerical simulations, J. Geophys. Res. **121**, 4157 (2016).
[130] M. N. Koshlyakov and A. S. Monin, Synoptic eddies in the ocean, Annu. Rev. Earth Planet. Sci. **6**, 495 (1978).
[131] D. B. Olson, Rings in the ocean, Annu. Rev. Earth Planet. Sci. **19**, 283 (1991).
[132] B. Galperin and S. Sukoriansky, Seasonal oceanic variability on submesoscales: Turbulence perspective, Ocean Dynamics (unpublished).
[133] B. Qiu, T. Nakano, S. Chen, and P. Klein, Submesoscale transition from geostrophic flows to internal waves in the northwestern Pacific upper ocean, Nat. Commun. **8**, 14055 (2017).
[134] Y. Xu and L.-L. Fu, The effects of altimeter instrument noise on the estimation of the wavenumber spectrum of sea surface height, J. Phys. Oceanogr. **42**, 2229 (2012).
[135] M. Tchilibou, L. Gourdeauand, R. Morrow, G. Serazin, B. Djath, and F. Lyard, Spectral signatures of the tropical Pacific dynamics from model and altimetry: A focus on the meso-/submesoscale range, Ocean Sci. **14**, 1283 (2018).
[136] P. Y. Le Traon, P. Klein, B. L. Hua, and G. Dibarboure, Do altimeter wavenumber spectra agree with the interior or surface quasigeostrophic theory? J. Phys. Oceanogr. **38**, 1137 (2008).
[137] J. G. Richman, B. K. Arbic, J. F. Shriver, E. J. Metzger, and A. J. Wallcraft, Inferring dynamics from the wavenumber spectra of an eddying global ocean model with embedded tides, J. Geophys. Res. **117**, C12012 (2012).
[138] D. Stammer, Global characteristics of ocean variability estimated from regional TOPEX/Poseidon altimeter measurements, J. Phys. Oceanogr. **27**, 1743 (1997).
[139] M. G. Scharffenberg and D. Stammer, Statistical parameters of the geostrophic ocean flow field, estimated by Jason-1-TOPEX/Poseidon tandem mission, J. Geophys. Res. **116**, C12011 (2011).
[140] L. S. Laurent, A. C. N. Garabato, J. R. Ledwell, A. M. Thurnherr, J. M. Toole, and A. J. Watson, Turbulence and diapycnal mixing in Drake Passage, J. Phys. Oceanogr. **42**, 2143 (2012).
[141] H. Sasaki, P. Klein, B. Qiu, and Y. Sasai, Impact of oceanic-scale interactions on the seasonal modulation of ocean dynamics by the atmosphere, Nat. Commun. **5**, 5636 (2014).
[142] Y. Kamidaira, Y. Uchiyama, H. Kawamura, T. Kobayashi, and A. Furuno, Submesoscale mixing on initial dilution of radionuclides released from the Fukushima Daiichi Nuclear Power Plant, J. Geophys. Res. **123**, 2808 (2018).
[143] R. Ferrari and D. L. Rudnick, Thermohaline variability in the upper ocean, J. Geophys. Res. **105**, 16857 (2000).
[144] P. S. Gay and T. K. Chereskin, Mean structure and seasonal variability of the poleward undercurrent off southern California, J. Geophys. Res. **114**, c02007 (2009).
[145] T. K. Chereskin, C. B. Rocha, S. T. Gille, D. Menemenlis, and M. Passaro, Characterizing the transition from balanced to unbalanced motions in the southern California Current, J. Geophys. Res. **124**, 2088 (2019).
[146] I. Lozovatsky, K. Shearman, A. Pirro, and H. J. S. Fernando, Probability distribution of turbulent kinetic energy dissipation rate in stratified turbulence: Microstructure measurements in the Southern California Bight, J. Geophys. Res. **124**, 4591 (2019).
[147] C. N. Flagg, G. Schwartze, E. Gottlieb, and T. Rossby, Operating an acoustic Doppler current profiler aboard a container vessel, J. Atmos. Ocean. Technol. **15**, 257 (1998).

[148] O. Bühler, M. Kuang, and E. G. Tabak, Anisotropic Helmholtz and wave-vortex decomposition of one-dimensional spectra, J. Fluid Mech. **815**, 361 (2017).
[149] C. Gourcuff, P. Lherminier, H. Mercier, and P. Y. Le Traon, Altimetry combined with hydrography for ocean transport estimation, J. Atmos. Ocean. Technol. **28**, 1324 (2011).
[150] B. Ferron, F. Kokoszka, H. Mercier, and P. Lherminier, Dissipation rate estimates from microstructure and finescale internal wave observations along the A25 Greenland-Portugal OVIDE line, J. Atmos. Oceanic Technol. **31**, 2530 (2014).
[151] A. Sánchez-Lavega, *An Introduction to Planetary Atmospheres* (CRC, Boca Raton, 2011).
[152] P. Hassanzadeh, P. S. Marcus, and P. Le Gal, The universal aspect ratio of vortices in rotating stratified flows: Fheory and simulation, J. Fluid Mech. **706**, 46 (2012).
[153] O. Aubert, M. Le Bars, P. Le Gal, and P. S. Marcus, The universal aspect ratio of vortices in rotating stratified flows: experiments and observations, J. Fluid Mech. **706**, 34 (2012).
[154] P. S. Marcus, S. Pei, C.-H. Jiang, and P. Hassanzadeh, Three-Dimensional Vortices Generated by Self-Replication in Stably Stratified Rotating Shear Flows, Phys. Rev. Lett. **111**, 084501 (2013).
[155] A. Salhi, A. Khlifi, and C. Cambon, Nonlinear effects on the precessional instability in magnetized turbulence, Atmosphere **11**, 14 (2020).
[156] B. Galperin, S. Sukoriansky, R. M. B. Young, R. Chemke, Y. Kaspi, P. L. Read, and N. Dikovskaya, in *Zonal Jets: Phenomenology, Genesis, and Physics*, edited by B. Galperin and P. L. Read (Cambridge University Press, Cambridge, 2019), pp. 220–237.
[157] J. C. McWilliams, Submesoscale currents in the ocean, Proc. R. Soc. A **472**, 20160117 (2016).
[158] G. Sahoo and L. Biferale, Energy cascade and intermittency in helically decomposed Navier-Stokes equations, Fluid Dyn. Res. **50**, 011420 (2018).
[159] H. Khatri, J. Sukhatme, A. Kumar, and M. K. Verma, Surface ocean enstrophy, kinetic energy fluxes, and spectra from satellite altimetry, J. Geophys. Res.: Oceans **123**, 3875 (2018).